

# A Reassessment of Hemispherical Power Asymmetry in CMB Temperature Data from Planck PR4 using LVE method

Sanjeev Sanyal<sup>1</sup>, Sanjeet K. Patel<sup>1</sup>, Pavan K. Aluri<sup>\*1</sup>, and Arman Shafieloo<sup>†2,3</sup>

<sup>1</sup>Dept. of Physics, Indian Institute of Technology (BHU), Varanasi - 221005, India

<sup>2</sup>Korea Astronomy and Space Science Institute (KASI), Yuseong-gu, 776 Daedeok daero, Daejeon 34055, Republic of Korea

<sup>3</sup>University of Science and Technology (UST), Yuseong-gu 217 Gajeong-ro, Daejeon 34113, Republic of Korea

November 26, 2024

## Abstract

We undertake a reassessment of one of the large angular scale anomalies observed in cosmic microwave background (CMB) temperature signal referred to as Hemispherical Power Asymmetry (HPA). For the present analysis we used SEVEM cleaned CMB maps from *Planck*'s 2020 final data release (public release 4/PR4). To probe HPA, we employed the local variance estimator (LVE) method with different disc radii ranging from  $1^\circ$  to  $90^\circ$ . It is reaffirmed that HPA is confined to low multipoles or large angular scales of the CMB sky. A dipole like anisotropy was found in the LVE maps with anomalous power for disc radii of  $2^\circ$  and upward up to  $36^\circ$  at  $\gtrsim 2\sigma$ . In the range  $4^\circ$  to  $10^\circ$  none of the 600 SEVEM CMB simulations were found to have a dipole amplitude higher than the data when using LVE method as proposed. Our emphasis here was to revalidate the LVE method in various ways for its optimal usage and probe the hemispherical power asymmetry in the form of a dipole modulation field underlying CMB sky. By and large, our results are in agreement with earlier reported ones with more detailed presentation of explicit and not-so-explicit assumptions involved in the estimation process. The above reported values fall in the reliability range of LVE method after this extensive re-evaluation. We conclude that the hemispherical power asymmetry still remains as a challenge to the standard model.

## 1 Introduction

Cosmological principle i.e., our universe is homogeneous and isotropic on large enough scales, is the concept on which the edifice of standard model of cosmology was built. Many tried to validate this principle using a variety of cosmological data. A powerful means to probe Cosmological principle is cosmic microwave background (CMB) radiation which was measured through ground as well as space-borne missions. So far three full-sky CMB experiments were conducted from space that provided maps of CMB anisotropies with varying precision [1, 2, 3]. These missions were aimed at measuring CMB with increasing precision particularly the temperature anisotropies, and many more are in commissioning or planning phase that will be operational in the future [4, 5, 6, 7]. The temperature and polarization anisotropy maps from WMAP and Planck satellite missions were studied extensively for any hints of deviations from statistical isotropy vis-a-vis the Cosmological principle. Such studies resulted in finding various

---

\*pavanaluri.phy@iitbhu.ac.in

†shafieloo@kasi.re.kr

anomalies that violate the assumption of isotropy. These anomalies were found in both WMAP and *Planck* data sets indicating their robustness across two different missions with different instrument properties and systematics.

From the first and three year data release of full-sky cleaned CMB maps from NASA’s WMAP satellite, an excess power in one hemisphere compared to the opposite hemisphere was found that violates statistical isotropy of CMB sky. This asymmetry centered around  $(\ell, b) = (225^\circ, -27^\circ)$  in galactic coordinates has come to be known as hemispherical power asymmetry (HPA) [8, 9]. Since then a variety of methods in real (pixel) and harmonic (multipole) space were devised to probe its presence and robustness [10, 11, 12, 13, 14, 15, 16, 17, 18]. It persisted in the final data release from the *Planck* mission (public release 4 or PR4). Its impact on inferred cosmological parameters were studied, for example, in Refs. [19, 20, 21]. Similar instances of isotropy violation were also seen in other astronomical data such as radio, quasar and supernova data [22, 23, 24, 25, 26]

In Ref. [27], a dipole modulation of otherwise isotropic CMB sky was proposed to describe the observed hemispherical power asymmetry. Thus we have,

$$\Delta T_{\text{obs}}(\hat{n}) \equiv \Delta T_{\text{mod}}(\hat{n}) = [1 + M(\hat{n})]\Delta T_{\text{iso}}(\hat{n}) = (1 + \vec{d} \cdot \hat{n})\Delta T_{\text{iso}}(\hat{n}) \quad (1)$$

where  $\Delta T_{\text{obs}}(\hat{n})/\Delta T_{\text{mod}}(\hat{n})$  is the observed/modulated (anisotropic) CMB sky, and  $\Delta T_{\text{iso}}(\hat{n})$  is the otherwise isotropic CMB temperature sky. Further,  $\vec{d} = A\hat{\lambda}$  where  $A, \hat{\lambda}$  are respectively the magnitude and direction of the modulating field ‘ $M(\hat{n})$ ’ that is taken to be purely dipolar in nature. No modes higher than a dipole in the modulating field were seen in the data [14].

## 2 Local variance estimator

Following the Cosmological principle (CP), specifically isotropy, the properties of the universe inferred from different directions should be consistent with each other within errorbars. For example, the number of galaxies in a given solid angle in any chosen direction or the properties of CMB anisotropies from any patch of any shape should have same properties irrespective of its location. In the standard cosmological model based on CP, CMB anisotropies are expected to be a statistically isotropic Gaussian random field.

Thus we consider a simple shape for the patch viz., a circular disc of some chosen radius at various locations covering the CMB sky to map the variance (our chosen property of CMB anisotropy field) computed locally from each of these circular regions. CMB maps are like a signal on a sphere and are digitized using the HEALPix pixelization scheme to represent data on a sphere<sup>1</sup>. The HEALPix parameter ‘ $N_{\text{side}}$ ’ is used to refer to the resolution of a CMB sky which are in powers of 2 i.e.,  $N_{\text{side}}=2^s$  where  $s = 0, 1, 2, 3$  and so on. The number of pixels in a HEALPix map are given by  $N_{\text{pix}}=12 \times N_{\text{side}}^2$ . So a higher  $N_{\text{side}}$  map denotes a high resolution map. Thus a CMB temperature anisotropy signal  $\Delta T(\hat{n})$  is equivalent to pixelized map  $\Delta T(p)$  where ‘ $p$ ’ is the pixel index whose pixel center is taken to be the direction of the incoming photon along  $\hat{n}$ .  $\Delta T(p)$  is the photon temperature anisotropy in the direction of pixel center corresponding to ‘ $p$ ’. Maps of CMB sky derived from NASA’s WMAP and ESA’s *Planck* satellite were usually made available at  $N_{\text{side}}=512$  and 2048 respectively.

Now, we can use a HEALPix grid of any  $N_{\text{side}}$  (typically lower than the original CMB map’s resolution) to map the variances computed locally by defining circular discs of different radii ‘ $r$ ’ at the corresponding pixel centers ( $\hat{N}$ ) uniformly covering the entire sky. Thus the local variance estimator (LVE) can be defined as [14],

$$\sigma_r^2(\hat{N}) = \frac{1}{N_p} \sum_{p \in r @ \hat{N}} (T(p) - \bar{T}_r)^2, \quad (2)$$

---

<sup>1</sup><https://healpix.sourceforge.io/>

where  $\bar{T}_r$  is the mean value of CMB fluctuations inside the circular disc of size ‘ $r$ ’, and ‘ $p$ ’ being the pixel indices of all pixels falling within the same disc centered in the direction  $\hat{N}$  of local variance map. Further ‘ $N_p$ ’ are the number of pixels in the circular disc from which variance is being computed locally. For brevity, we used  $T(p)$  instead of  $\Delta T(p)$  to denote CMB temperature anisotropies.

Following Eq. (1), the LVE map of a dipole modulated CMB sky, upto first order in ‘ $A$ ’ is given by,

$$\sigma_{\text{obs}}^2(\hat{N}) \approx \sigma_{\text{iso}}^2(\hat{N})(1 + 2A\hat{\lambda} \cdot \hat{N}). \quad (3)$$

Assuming that the amplitude of isotropy violating modulation field to be small, we considered terms only up to first order in ‘ $A$ ’ in the above equation. So an LVE map’s dipole amplitude will be *twice* that of a dipole modulated CMB map to leading order.

Thus in order to probe the properties of the LVE map for any signatures of isotropy violation, we can define a normalized variance map as,

$$\xi(\hat{N}) = \frac{\sigma_{\text{obs}}^2(\hat{N}) - \langle \sigma_{\text{iso}}^2(\hat{N}) \rangle}{\langle \sigma_{\text{iso}}^2(\hat{N}) \rangle} \quad (4)$$

where  $\langle \sigma_{r,\text{iso}}^2(\hat{N}) \rangle$  is the expected bias in an LVE map due to random fluctuations in a particular realization of CMB sky such as our universe. It is computed from simulated CMB maps based on standard cosmological model incorporating appropriate measurement artifacts such as detector noise, beam and pixel window effects specific to an instrument. Accordingly, the normalized LVE map of a dipole modulated CMB sky following Eq. (1) and (3) will be,

$$\xi(\hat{N}) \equiv 2A\hat{\lambda} \cdot \hat{N}. \quad (5)$$

There are some practical consideration in employing the local variance estimator (LVE). First, irrespective of the cleaning procedure used to extract *clean* CMB sky signal from raw satellite data, there will always be residual contamination in the cleaned CMB maps thus obtained. This is particularly true in regions closer to galactic plane where foreground emission of astrophysical origin is strong. Hence in order not to bias our inferences, a galactic mask is used. So the circular disc is taken in conjugation with the galactic mask omitting those pixels or regions of the sky, where the recovered CMB signal is deemed potentially contaminated. Then, to compute our estimator reliably i.e., local variances, we do not consider variances from circular discs in which 90% or more fraction of the pixels compared to those in a full circular disc get omitted as a consequence of masking in our analysis.

To derive LVE maps, we select discs of different sizes that allows us to probe any angular/multipole dependence of the amplitude of the underlying (dipole) modulation field. The angular scale of a CMB fluctuation, say  $\theta$ , is related to the multipole as  $l = 180^\circ/\theta$ . Choosing a disc radius of size ‘ $r$ ’ to compute local variances, we are filtering the CMB map upto a multipole of order  $l \sim 180^\circ/r$ . Correspondingly the amplitude of modulation will be  $\equiv A_l$ . If the underlying modulation field is same at all scales  $A_l = A$  (some constant to be determined from LVE maps using different disc radii).

Now, even if the CMB sky is isotropic (in data or a simulation), there will always be a random dipole component (and other higher order modes) to be found in the corresponding LVE map. Thus, following Eq. (1), we have :

$$\langle d_i \rangle = 0 \quad \text{and} \quad \langle d_i^2 \rangle \neq 0, \quad \forall \quad i = x, y, z, \quad (6)$$

for the components of the dipole in the modulating field. Since the amplitude is given by,

$$A = \sqrt{d_x^2 + d_y^2 + d_z^2}, \quad (7)$$

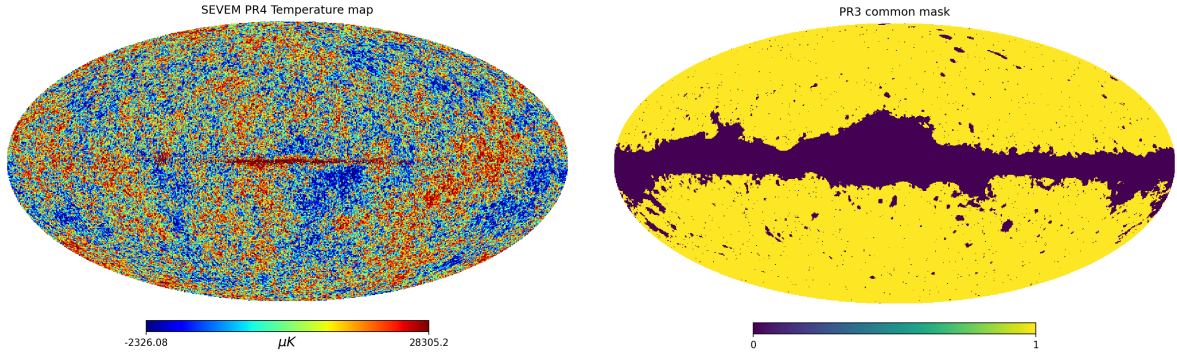


Figure 1: The SEVEM cleaned CMB map from *Planck*'s PR4 data release (*top left*), the PR3 *common* mask recommended for use with PR4 cleaned CMB maps (*top right*) are shown here.

assuming only a dipole like component in the modulating field, it will always be non-zero. By a simple transformation one can show that the dipole power, say,  $C_1$  is related to the dipole amplitude,  $A$ , as  $C_1 = 4\pi A^2/9$ . Therefore, to get the *correct* dipole power underlying the CMB sky, one should subtract expected random dipole power,  $\langle C_{1,\text{iso}} \rangle$ , that is equivalent to a noise term i.e.,  $C_{1,\text{corr}} = C_{1,\text{obs}} - \langle C_{1,\text{iso}} \rangle$  or equivalently,

$$A_{\text{corr}}^2 = A_{\text{obs}}^2 - \langle A_{\text{iso}}^2 \rangle. \quad (8)$$

If one is employing multipole space estimators, the *unbiased* estimate of the dipole amplitude will be given by

$$A_{\text{corr}} = 1.5 \sqrt{(C_{1,\text{obs}} - \langle C_{1,\text{iso}} \rangle) / \pi}. \quad (9)$$

In order to estimate the dipole in an LVE map we use HEALPix function `remove_dipole` which returns the dipole amplitude, ‘ $A$ ’, as well as its direction  $(\theta, \phi)$  (or equivalently  $(\ell, b)$ ) in galactic coordinates which is the coordinate system of the input CMB map(s) used in the present study.

### 3 Data and Complementary simulations

#### 3.1 Observed CMB maps and galactic mask used

We use cleaned CMB maps from *Planck*'s public release 4 (PR4) data that were derived using the SEVEM procedure. The SEVEM cleaning procedure is one of the variants of the most commonly used internal linear combination (ILC) methods in real (pixel) space [28, 29]. It involves forming foreground “templates” by taking differences of observed raw satellite maps (in thermodynamic units) from specific frequency channels that can serve as a proxy for one or more of the foregrounds present in the microwave sky. As a result of such subtraction, the difference maps don't have any CMB signal in them. These difference maps are then subtracted with appropriate weights from rest of the observed maps (at other frequencies that are not used in taking the difference maps to form foreground templates) to get a *cleaned* CMB map. For more details regarding the SEVEM method, the reader may consult the original papers cited above.

The SEVEM cleaned CMB map from the entirety of *Planck*'s observations in different (a total of nine) frequency bands is produced at  $N_{\text{side}}=2048$  with a detector beam resolution given by a Gaussian window function of  $FWHM = 5'$  (arcmin). No matter how good a cleaning algorithm may be, in regions of strong galactic emission, the recovered CMB signal is not reliable and hence omitted from any kind of cosmological analysis. In order to omit such regions, *Planck* collaboration provided a confidence mask along with the CMB map derived using SEVEM procedure, as is the case with any other cleaning procedure employed by *Planck*. However a

combined mask referred to as *common* mask was also provided by *Planck* collaboration for use with any of the cleaned CMB maps that it produced. These masks are provided as a binary map with  $\{0, 1\}$  where pixels/regions that should be omitted are represented by ‘0’ and the allowed pixels/regions are denoted by ‘1’. The common mask has, expectedly, lower non-zero sky fraction, often denoted by the symbol  $f_{\text{sky}}$ , compared to individual cleaning method (component separation) specific CMB confidence masks. We use the PR3 common mask, as recommended [29], that has an available sky fraction of  $f_{\text{sky}} \approx 77.94\%$ .

In Fig. [1], we show the SEVEM cleaned CMB map from *Planck*’s PR4 and the recommended *Planck*’s PR3 *common* mask for temperature analysis of PR4 data.

### 3.2 Simulations

Among the suite of data products released by *Planck* as part of PR4, simulations corresponding to SEVEM CMB maps are also provided that are referred to as FFP (Full Focal Plane) simulations, specifically the FFP12 set of CMB realizations along with noise. CMB and noise maps are simulated at the nine frequency channels in which *Planck* made observations with appropriate beam and pixel window effects. A total of 600 sets of nine frequency specific CMB and noise maps were provided as part of *Planck* PR4. This is less than the usual number of 1000 simulations that were provided with each of the earlier *Planck* public releases. Each of these simulation sets have nine channel maps that are combined using the same weights that were applied on data to do foreground reduction. Thus a total of 600 CMB and noise simulations are provided mimicking the properties of observed CMB map. These have the same beam and HEALPix resolution as the data viz., a beam resolution given by a Gaussian beam of  $FWHM = 5'$  and  $N_{\text{side}}=2048$ . These are made available on NERSC facility<sup>2</sup> and *Planck* legacy archive<sup>3</sup> (PLA).

The local variance estimator method is validated and used in various studies including the *Planck* team’s tests of isotropy and statistical consistency of CMB sky with standard model expectations based on Cosmological principle [30]. However we validate the method again, while also presenting some of the not so explicitly demonstrated aspects of LVE methodology.

We generated three sets of CMB realizations from the *Planck* provided FFP12 simulation ensemble. The first set i.e., the 600 SEVEM FFP simulations correspond to isotropic random realizations of CMB sky based on standard cosmological model. Their spherical harmonic coefficients are given by  $a_{lm}^{\text{iso}} = b_l^{5'} p_l^{2048} a_{lm}^{\text{CMB}}$ , where  $b_l^{5'}$  corresponds to the  $5'$  (arcmin) Gaussian beam transfer function and  $p_l^{2048}$  is the pixel window function for  $N_{\text{side}}=2048$  due to the finite size of the HEALPix sky discretization scheme. From these isotropic realizations, we generate two sets of dipole modulated simulations for our purpose of revalidation of LVE method.

The second set of simulations are dipole modulated maps at all scales with a fixed amplitude along a particular direction as previously found in the data. To generate these “*pure-dm*” simulations, first we get the spherical harmonic coefficients,  $a_{lm}^{\text{iso}}$ , of FFP12 CMB mock maps using `map2alm` routine of HEALPix. These  $a_{lm}^{\text{iso}}$  are then deconvolved with corresponding beam smoothing ( $b_l^{5'}$ ) and pixel window function ( $p_l^{2048}$ ) to apply a dipole modulation according to Eq. (1) with an amplitude of  $A = 0.072$  and directed along  $(\ell, b) = (221^\circ, -20^\circ)$  in galactic coordinates [30] on the deconvolved CMB map. Finally, we convolve this modulated CMB map with the same  $b_l$  and  $p_l$ . Thus we obtain dipole modulated CMB maps with the same amplitude at all scales using the `alm2map` routine of HEALPix.

A third set of simulations were also generated to simulate the observed case of dipole modulation in data, where the modulation is present only on large angular scales of the CMB sky up to  $l \sim 64$  [31]. In order to simulate such “*low-l-dm*” maps, we combine the spherical harmonic coefficients of an FFP12 isotropic SEVEM CMB map and a *pure-dm* map with the same

<sup>2</sup><http://crd.lbl.gov/cmb-data>

<sup>3</sup><https://pla.esac.esa.int/>



$N_{\text{side}}$	32	16	8	4	2	1
$N_{\text{pix}}=12 \times N_{\text{side}}^2$	12288	3072	768	192	48	12
Pixel size ( $\sqrt{4\pi/N_{\text{pix}}}$ )	1.83°	3.66°	7.33°	14.66°	29.32°	58.63°
Disc size ( $r^\circ$ )	1°	2°	4°	8°	16°	32°

Table 1: Pixel sizes (PS) corresponding to various **HEALPix** resolutions characterized by the  $N_{\text{side}}$  parameter and the approximate disc radii ( $\sim PS/2$ ) that could be used with that **HEALPix** grid to match those pixel sizes are listed here.

index using a “cosine” filter defined in multipole space for smooth transition between dipole modulated  $a_{lm}$  at low multipoles to isotropic  $a_{lm}$  at high multipoles. The filter is defined as,

$$f_l = \begin{cases} 1 & l < l_1 \\ \frac{1}{2} \left[ 1 + \cos \left( \pi \frac{l-l_1}{l_2-l_1} \right) \right] & l_1 \leq l \leq l_2 \\ 0 & l > l_2 \end{cases} \quad (10)$$

choosing  $l_1 = 60$  and  $l_2 = 70$  for our purpose. Thus a *low-l-dm* CMB map with dipole modulation confined to large angular scales is generated as,

$$a_{lm}^{\text{low-l-dm}} = f_l a_{lm}^{\text{pure-dm}} + (1 - f_l) a_{lm}^{\text{iso}} \quad (11)$$

where  $a_{lm}^{\text{low-l-dm}}$ ,  $a_{lm}^{\text{pure-dm}}$ ,  $a_{lm}^{\text{iso}}$  are the spherical harmonic coefficients of low multipole dipole modulated, all scale dipole modulated and isotropic CMB realizations respectively. These  $a_{lm}$ ’s are then converted back to pixel domain (using `alm2map` routine of **HEALPix**).

Finally, all these three sets of CMB realizations are added with FFP12 noise maps having the same index to get the final noisy (an)isotropic CMB realizations. The nine noise maps corresponding to nine frequency channels of a particular simulation (index) were also combined by the *Planck* collaboration in a way similar to the **SEVEM** FFP12 CMB realizations using the same data derived weights for foreground cleaning.

## 4 Analysis and Results

### 4.1 Validation

Here we present a (re)validation of the LVE method for probing the dipole modulation signal supposedly underlying the observed CMB sky.

In the first application of local variance estimator method [14], a **HEALPix** grid of  $N_{\text{side}}=16$  was used whose pixel centers uniformly cover the entire sky to map the locally computed variances. One would want to use temperature anisotropy information (pixel values of digitized CMB map) from disjoint regions so that they are uncorrelated with each other. However, depending on the size of the disc radius used with a fixed  $N_{\text{side}}(=16, \text{ in this case})$ , the locally computed variances will have overlapping pixels from adjoining regions, making them correlated. It is also possible that the circular discs used to compute variances locally are smaller than the pixel size of the chosen **HEALPix** grid of the LVE map itself and doesn’t make use of all the pixels in original CMB map (that is usually at a higher resolution, which is at  $N_{\text{side}}=2048$  in our case compared to  $N_{\text{side}}=16$  of the LVE map).

One resolution to this situation is to choose the region covered by the pixel of a lower  $N_{\text{side}}$  **HEALPix** grid as mask to map local variances, by upgrading the LVE map’s grid with one pixel at a time to that of the input CMB map. This will keep the regions disjoint and the locally computed variances uncorrelated in estimating the underlying dipole modulation signal. However as shown in Table 1, this can be done only for a few select disc radii that matches

Disc Radius ( $r$ )	$N_{\text{side}}$	Pixel Size, PS	$\sqrt{2} \times \text{PS}$
1°	32	1.83°	2.59°
2°	16	3.66°	5.18°
4°, 6°	8	7.33°	10.36°
8°, 10°, 12°, 14°	4	14.66°	20.73°
16°, 18°, 20°, 24°, 28°, 32°, 36°, 40°, 50°, 60°, 70°, 80°, 90°	2	29.32°	41.46°

Table 2: Selection of  $N_{\text{side}}$  with different disc sizes. Treating each **HEALPix** pixel to be a square of size (side) given by  $\sqrt{4\pi/N_{\text{pix}}}$  where  $N_{\text{pix}} = 12 \times N_{\text{side}}^2$ . This is denoted by ‘PS’. Size of the pixels as measured along the diagonal of such a square is  $\sqrt{2} \times PS$ . These numbers help us in choosing appropriate **HEALPix** grid to generate LVE maps for a particular disc radius with minimal to no overlaps in the LVE maps.

with the pixel size of LVE map’s  $N_{\text{side}}$ . These pixel sizes are estimated assuming the **HEALPix** pixels to be a square of side  $\sqrt{4\pi/N_{\text{pix}}} \times 180^\circ/\pi$  in degrees, where  $4\pi$  is the area of the entire spherical surface (of a unit sphere) that is divided into  $N_{\text{pix}}$  pixels using **HEALPix**.

If one wishes to undertake a detailed study of HPA as a function of angular scale (or equivalently as a function of multipole,  $A_l$ ), then LVE maps are computed with different choices of disc radii covering the entire CMB sky. Since local variances are computed from overlapping regions for different  $N_{\text{side}}$  and disc radii ( $r$ ) choices other than those listed in Table 1, correlations between them will be unavoidable. However, to minimize the correlations in an LVE map, it would be useful to define a **HEALPix** grid to derive an LVE map from a CMB map that has varying  $N_{\text{side}}$  to match the chosen disc radii as much as possible. In Table 2, we show the different  $N_{\text{side}}$  values chosen to match the disc radius used to compute an LVE map in the present work, instead of using a fixed  $N_{\text{side}}=16$ , say. It also allows to probe anisotropy at smaller scales by using a suitably higher  $N_{\text{side}}$  grid for an LVE map for signals such as the Doppler boosting of CMB, whose signature is evident readily at small angular scales, as a result of coupling between adjacent multipoles [32].

Let  $p$  and  $p'$  be any two pixel indices of a normalized LVE map,  $\xi(\hat{N})$ , estimated for some choice of disc radius ‘ $r$ ’, and let  $C_{pp'}$  denotes the covariance matrix. Then the covariance and the corresponding correlation matrix are defined in the usual way as,

$$C_{pp'} = \langle \xi_{\text{iso}}(p)\xi_{\text{iso}}(p') \rangle - \langle \xi_{\text{iso}}(p) \rangle \langle \xi_{\text{iso}}(p') \rangle, \quad (12)$$

$$\tilde{C}_{pp'} = \frac{C_{pp'}}{\sqrt{C_{pp}C_{p'p'}}}. \quad (13)$$

The correlation matrix  $\tilde{C}_{pp'}$  is defined such that the covariance matrix elements are normalized with respect to the diagonal elements, which are dominant and positive. The correlation matrix elements consequently range between  $-1$  and  $+1$ . Here  $\xi_{\text{iso}}$  stands for normalized LVE maps from the FFP12 isotropic (**SEVEM**) CMB realizations added with noise. In Fig. [2], we show the covariances ( $C_{pp'}$ ) in a normalized LVE map estimated for a disc radius of  $r = 16^\circ$  but at different **HEALPix** resolutions of  $N_{\text{side}}=2,4,16$  in the *top* panel. In the same figure, the corresponding correlation matrices ( $\tilde{C}_{pp'}$ ) are shown in the *bottom* panel to highlight the relative strength of the covariance matrix elements.

From Fig. [2], it is clear that an LVE map’s  $N_{\text{side}}$  should be chosen such that its pixel size matches with the disc radius used to compute the variances of a CMB map locally. In doing so we can keep the LVE map’s covariance matrix predominantly diagonal, if not diagonal, as is obvious from the first two panels (top or bottom) of Fig. [2]. Otherwise there will be correlations across several diagonals as can be seen from the third panel (top or bottom) of Fig. [2], that have to be accounted for in estimating the underlying modulation (or any anisotropy) field.

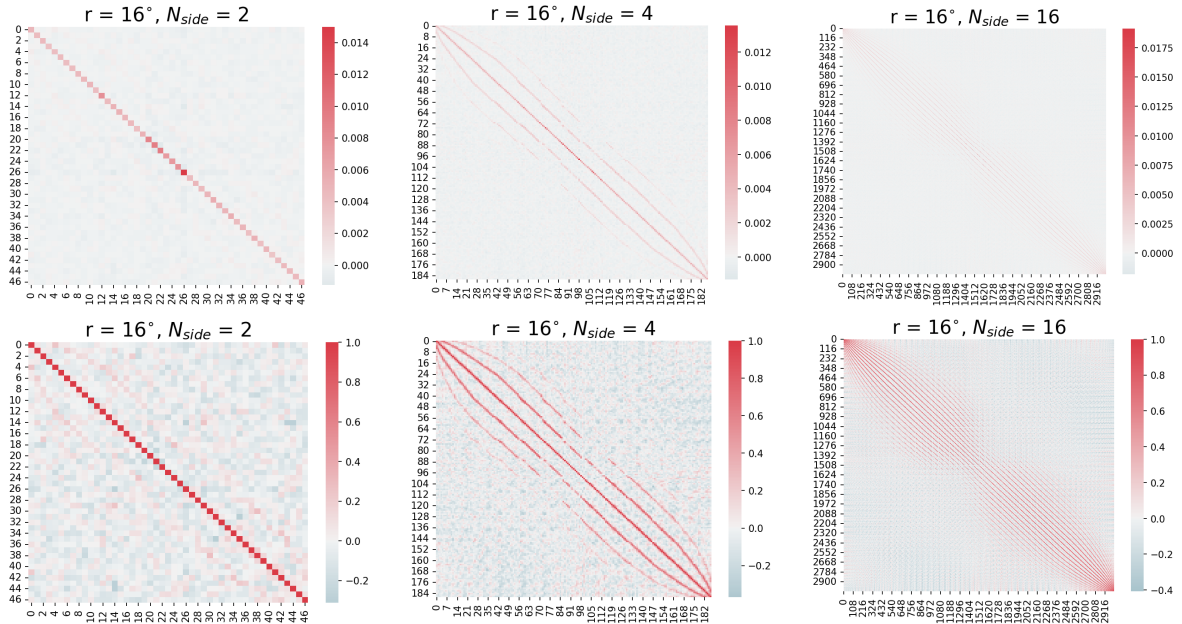


Figure 2: *Top*: Covariance matrices  $C_{pp'}$  as defined in Eq. (12) corresponding to normalized LVE maps generated at  $N_{\text{side}}=2, 4,$  and  $16$  but for a particular disc radius  $r = 16^\circ$ . *Bottom*: Correlation matrices,  $\tilde{C}_{pp'}$ , (normalized covariance matrices) as defined in Eq. (13) corresponding to the same disc radius but for different  $N_{\text{side}}$  LVE maps as shown in the *top* panels.

For the larger disc radii, we fix  $N_{\text{side}}=2$  to estimate LVE maps which is sufficient and also computationally fast. Thus we use different  $N_{\text{side}}$ 's to estimate LVE maps for different choices of disc radii as listed in Table 2, to keep the correlations across pixels minimal. This exercise also points out that the variances of an LVE map's pixels are different as can be seen from the diagonals of *top* panels of Fig. [2]. It is indeed known that the variances of a Gaussian random variable themselves follow a  $\chi^2$  distribution. So they will be different. Thus we use these variances as weights (inverse variance weighting) to better estimate the dipole modulation field (using the `remove_dipole` functionality of `HEALPix`).

These covariance matrices were obtained using the 600 `SEVEM` CMB realizations including noise provided as part of *Planck* PR4. For each disc radius, we estimated the covariance matrix from the normalized LVE maps for that chosen disc radius as derived from *isotropic* FFP12 simulation set. These were used in the (re)evaluation of the LVE method using “pure-dm” and “low-l-dm” CMB ensembles. We remark that the dipole modulation field's amplitude or direction derived using the `remove_dipole` function of `HEALPix` as-it-is only differs nominally from those derived using the same function with diagonal elements of the covariance matrices,  $C_{pp'}$ , for inverse variance weighing to fit the dipole. We show some representative plots in Fig. [A.1] and [A.2] in Appendix A. The distribution of recovered dipole amplitude and direction of LVE maps are essentially same in both the cases where a fixed `HEALPix` grid of  $N_{\text{side}}=16$  is used for all disc radii or a different  $N_{\text{side}}$  grid was chosen for different choices of disc radii. In the rest of the paper, knowing that the variance of different pixels in an LVE map are different, we use diagonal elements from the covariance matrices as weights in computing the dipole component.

From the three simulation ensembles (viz., the isotropic `SEVEM` CMB realizations as they are provided by the *Planck* collaboration (iso), and all scale dipole modulated CMB maps (pure-dm), and low- $l$  only modulated CMB maps (low-l-dm) that we generated), we present the recovered dipole amplitudes in Fig. [3] for the different disc radii listed in Table 2. We used the inverse variance weighting to compute the dipole amplitude. It is clear from the figure that the distribution/scatter in the recovered amplitudes are similar, except for low radii where they



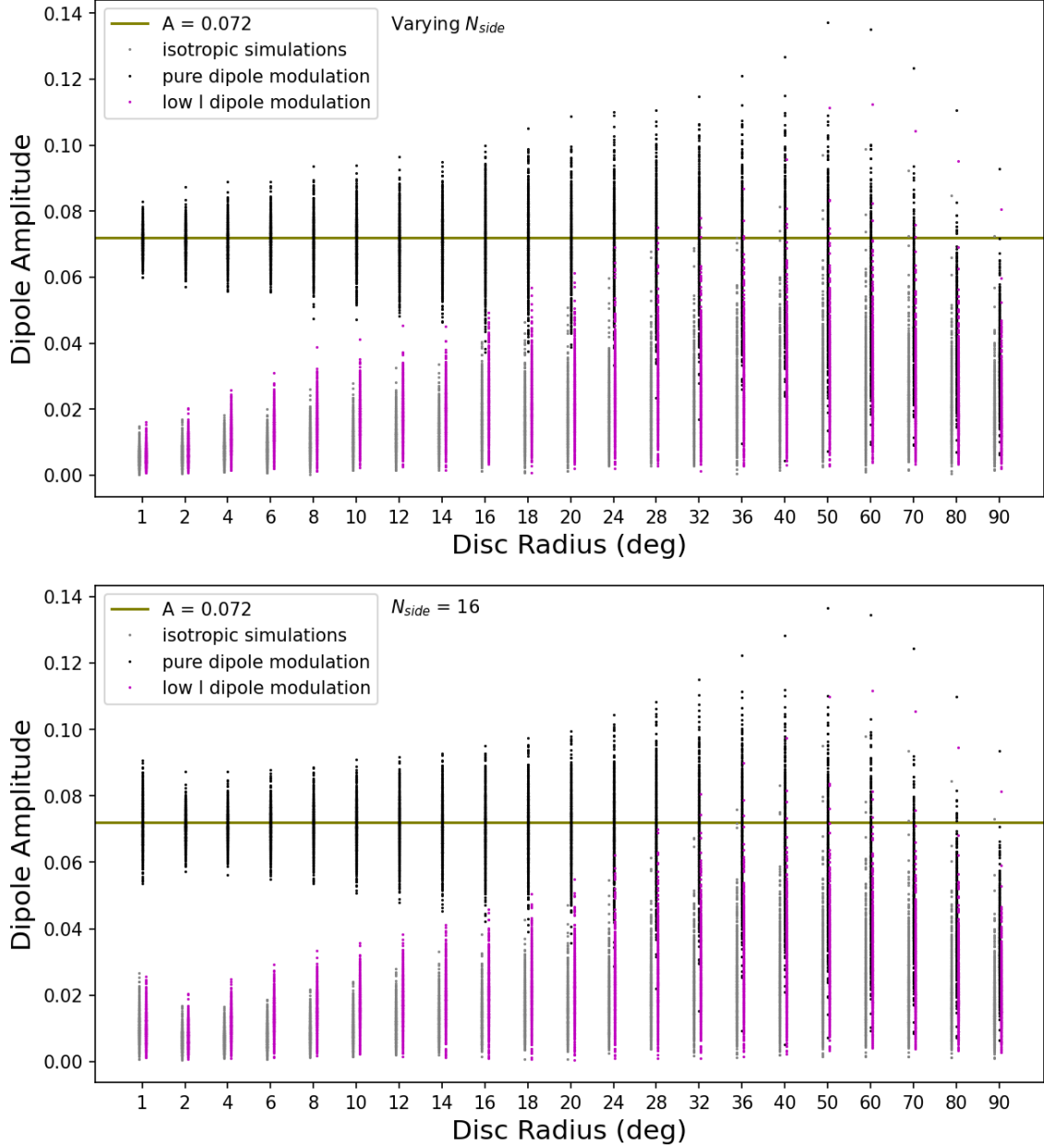


Figure 3: *Top* and *Bottom* panels depict the distribution of dipole amplitudes from isotropic (gray), low- $l$  dipole modulation (magenta) and pure dipole modulation (black) simulation ensembles evaluated from normalized local variance maps with varying  $N_{side}$  and fixed  $N_{side}=16$  resolutions, respectively.

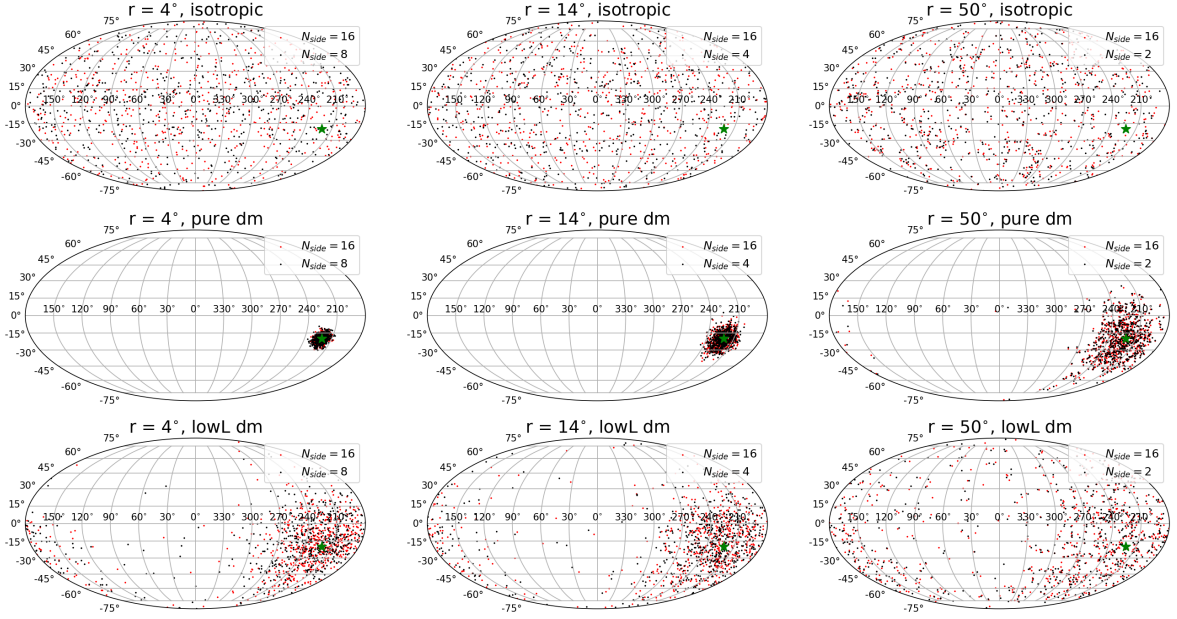


Figure 4: Recovered dipole modulation directions in LVE maps for some select disc radii as indicated. The *top*, *middle* and *bottom* rows comparatively show the LVE maps' dipole directions from isotropic, pure-dm and low- $l$ -dm simulation sets using fixed  $N_{\text{side}}=16$  (red dots) and varying  $N_{\text{side}}$  (black dots) for deriving LVE maps. These dipoles in LVE maps are fit using Inverse variance weighting using the `remove_dipole` functionality of HEALPix.

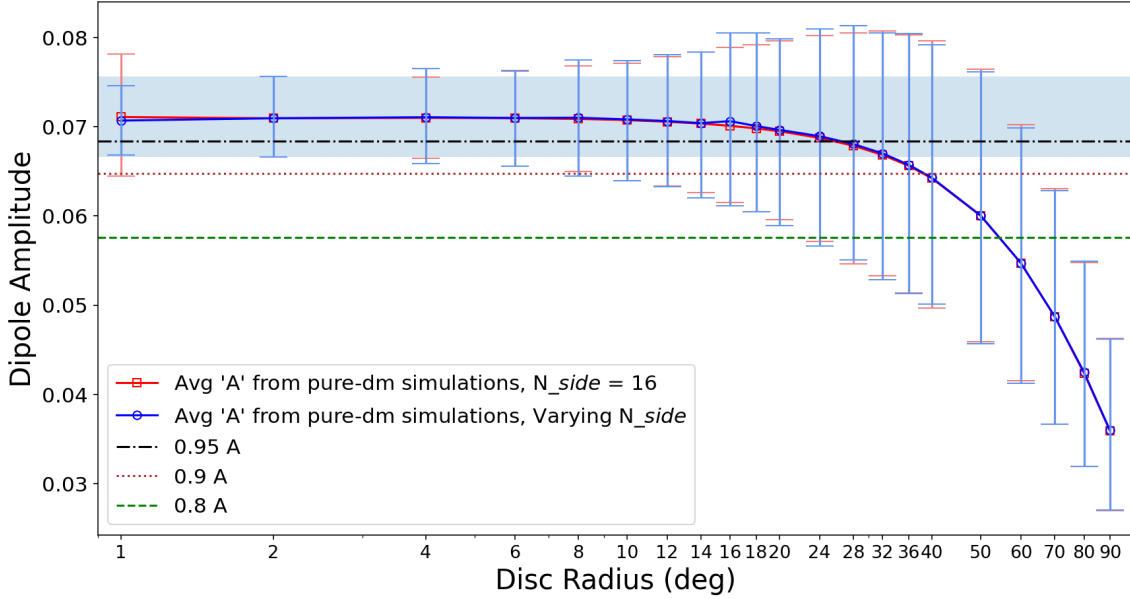


Figure 5: Mean dipole amplitude recovered from LVE maps of pure-dm simulation ensemble with corresponding errorbars. LVE computed with a fixed  $N_{\text{side}}=16$  and varying  $N_{\text{side}}$  are shown in red square and blue circle point types. The black, brown and green horizontal lines correspond to different tolerance levels, specifically, 5%, 10% and 20% decrement in recovered dipole amplitude compared to injected amplitude of  $A = 0.072$ . The light blue band corresponds to  $1\sigma$  error from LVE maps for disc size  $r = 2^\circ$  where the  $N_{\text{side}}$  for the two cases of fixed  $N_{\text{side}}$  and varying  $N_{\text{side}}$  coincides i.e.,  $N_{\text{side}}=16$  in generating LVE maps. Wherever these lines/band cross the mean dipole amplitude curve, they indicate the disc radius beyond which the LVE method may not be appropriate for that tolerance level in the recovered dipole amplitude from LVE maps.

are visibly different. We expect this would lead to a different  $p$ -values profile as a function of disc radii between the two scenarios for LVE maps with fixed  $N_{\text{side}}=16$  and varying  $N_{\text{side}}$ . The corresponding dipole directions in LVE maps, from the three different simulations ensembles created, for some select disc radii are shown in Fig. [4]. The mean of the recovered dipole is in agreement with the injected dipole modulation field from pure-dm maps.

Now, we note some observations about the LVE method.

- From Fig. [3] (as also presented originally in Ref. [14]), the recovered dipole amplitude of hemispherical power asymmetry is lower than the injected dipole amplitude for larger disc radii. We again show Fig. [3] in an alternate way in Fig. [5]. In this figure, mean of the recovered dipole amplitude from the fixed  $N_{\text{side}}$  and varying  $N_{\text{side}}$  cases are shown together. For  $r \gtrsim 16^\circ$ , the mean of the recovered dipole amplitudes starts to deviate (towards lower values) from the injected dipole amplitude of  $A \approx 0.07$  though the error bars also increase. This indicates a breakdown of the LVE method.
- Specifically, for large disc radii, the assumption of dipole being the largest angular scale feature on the sky as a background in Eq. (2) and (3) fails, and the expected variance  $\sigma_{\text{iso}}^2$  cannot be taken out (as is the case for smaller disc radii compared to the dipole of the modulation field).
- Various horizontal lines in Fig. [5] suggest a cutoff disc size for employing LVE method depending on one's tolerance level in estimating the dipole amplitudes. If one deems a 5% decrement in the mean of the recovered dipole amplitudes (i.e.,  $\sim 0.95A$ ) as tolerable with respect to the injected dipole amplitude, while being consistent with it within errorbars, a maximum disc radius of  $\sim 28^\circ$  can be employed where the *black* dash-dotted line crosses the mean dipole amplitude curve. If one can tolerate a decrement of 10% and 20% decrement i.e.,  $0.9A$  and  $0.8A$  indicated by a *brown* dotted line and a *green* dashed line respectively in the mean dipole amplitude recovered but nevertheless contains the injected dipole amplitude 'A' within error bars, then we can go up to a disc size of  $\sim 40^\circ$  and  $\sim 55^\circ$  respectively. The *blue band* band corresponds to  $1\sigma$  uncertainty in the recovered dipole amplitude for disc radius  $r = 2^\circ$  where  $N_{\text{side}}$  of LVE maps for both cases is same. For this level of tolerance (blue band) in the deviation from injected dipole amplitude, we find that LVE maps should be estimated up to a maximum disc radius of  $r \sim 32^\circ$ .
- The error bars on the recovered dipole amplitude increases with increasing disc radius where the assumption in Eq. (3) breaks down. So we should use the LVE method to probe isotropy violation underlying CMB sky such as HPA to only lower disc radius to get a reliable estimate. Also note that these uncertainties folds in the large cosmic variance associated with low multipoles.
- Here one can ask a followup question as to whether the maximum disc radius of reliability of LVE method is dependent on the level of anisotropy? To address this, we simulated dipole modulated (pure-dm) simulations with two other choices of dipole amplitudes viz.,  $A = 0.05$  and  $A = 0.1$ . For this exercise, LVE maps with varying  $N_{\text{side}}$  were computed from these pure-dm simulations. The results are presented in Fig. [6]. As is obvious from the figure, for lower levels of isotropy violation, in this case HPA modeled as dipole modulation of otherwise isotropic CMB sky, the LVE method is reliable up to a higher disc radius compared to stronger levels of isotropy violation where the method breaks down (Eq. 3 and 5) at a relatively lower disc radii. Specifically, for  $A = 0.05$  the LVE method holds up to a choice of  $r \approx 50^\circ$ , whereas for an anisotropy level of  $A = 0.1$  it is reliable up to only  $r \approx 34^\circ$  to probe HPA with a tolerance level for 10% deviation in the mean recovered dipole amplitude from simulations, but however consistent with the injected dipole amplitude within errorbars.

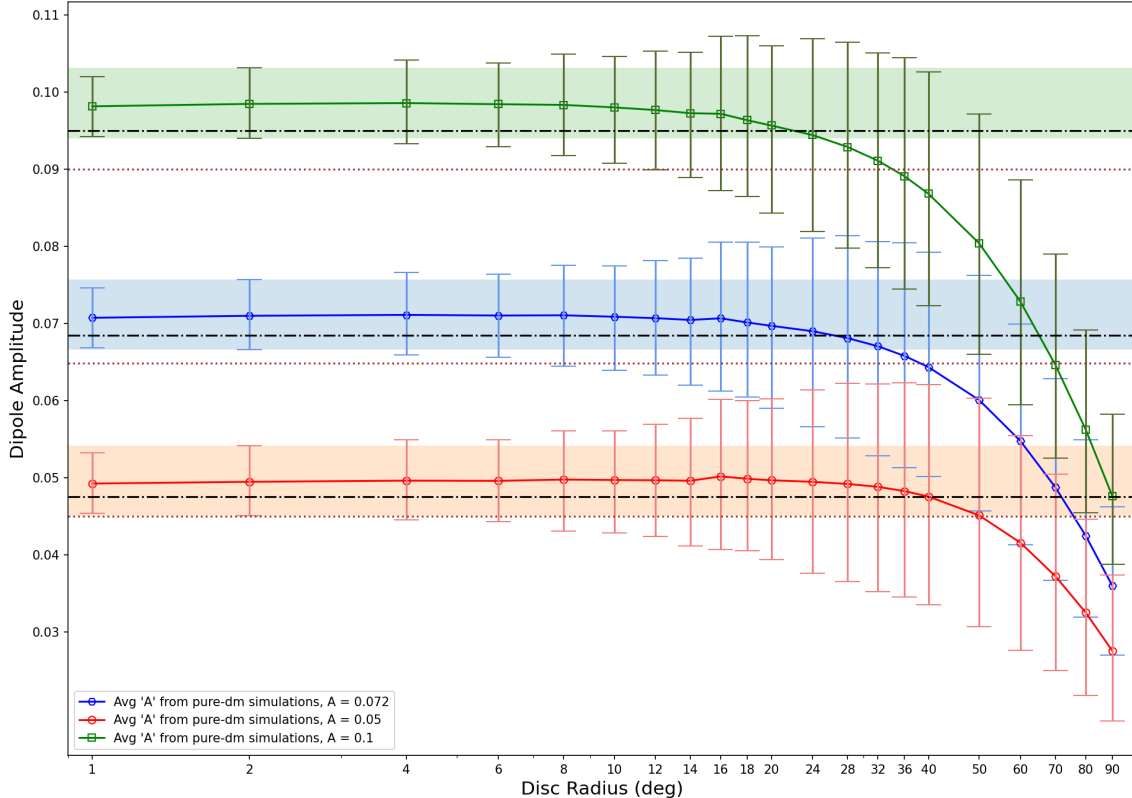


Figure 6: Evaluating the maximum disc radius that can be chosen to use the LVE method for different levels of anisotropy i.e., dipole modulation amplitudes of  $A = 0.1$ ,  $0.072$  and  $0.05$  underlying a CMB sky. We clearly see a dependence in the LVE method’s reliability range of disc radii on the strength of anisotropy. For a 10% admissible level of deviation from mean recovered dipole amplitude with respect to the injected value, but however consistent with it within errorbars, LVE method can be employed choosing a maximum disc radius of  $r \approx 34^\circ$ ,  $40^\circ$  and  $50^\circ$  for a dipole modulation amplitude of  $A = 0.1$ ,  $0.072$  and  $0.05$  respectively. Only pure dipole modulated CMB realizations with noise were used for this evaluation. Further the corresponding LVE maps were derived using the varying  $N_{\text{side}}$  approach.

With this extensive re-evaluation of LVE method using simulations from *Planck* PR4, we proceed with presentation of results from analyzing the data. We note that using varying  $N_{\text{side}}$  not only do we get to compute local variances from nearly non-overlapping regions of the CMB sky under study, but also at reduced computational cost.

## 4.2 Data analysis and Results

As already mentioned in the previous section, we will be using the diagonal elements of the covariance matrices, derived using FFP12 isotropic simulation ensemble from *Planck* PR4, as weights for inverse variance weighting to fit the dipole in LVE maps. We use the `remove_dipole` function of `HEALPix` package. Further, we will be presenting results from both the cases where a fixed  $N_{\text{side}}=16$  and varying  $N_{\text{side}}$  `HEALPix` grid were used to derive LVE maps from data/simulations, and make comparative statements.

In Fig. [7], LVE maps from *Planck* PR4 SEVEM solution of cleaned CMB sky for some select disc radii are shown. In this figure, we chose LVE maps corresponding to disc radii  $r = 4^\circ$ ,  $14^\circ$ , and  $50^\circ$  for illustration. Both cases of fixed  $N_{\text{side}}=16$  (*top* row) and varying  $N_{\text{side}}$  to match different choices of disc radii (*bottom* row) are shown in the figure. Note that these are normalized variance maps as defined in Eq. (4).

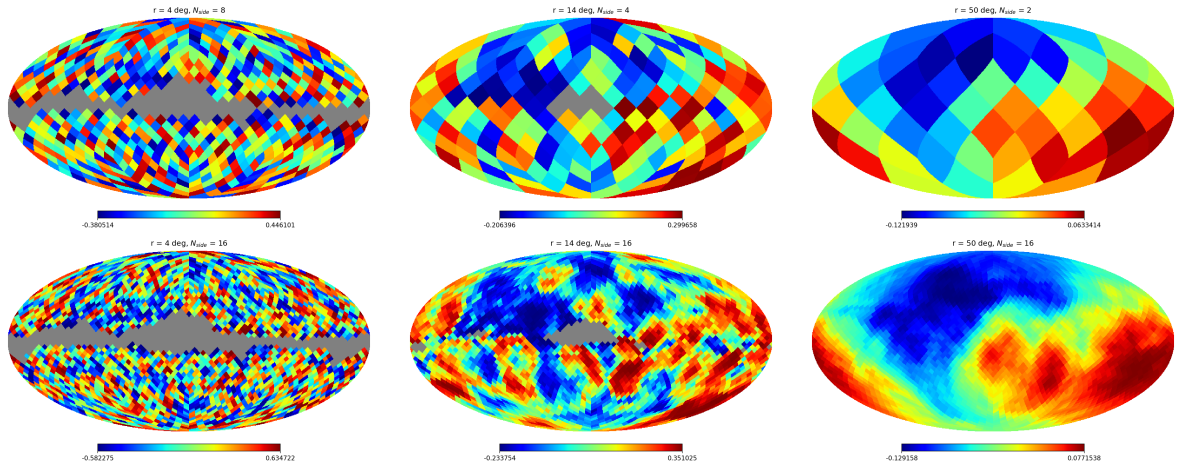


Figure 7: Normalized LVE maps (per Eq. (2) and (4)) corresponding to SEVEM CMB solution from *Planck* PR4 data for some select disc radii are shown here. In the *top* row, LVE maps with varying  $N_{\text{side}}$  grid for obtaining LVE maps are shown, and in the *bottom* row the same are shown for a fixed  $N_{\text{side}}=16$  used in deriving LVE maps. From *left to right* the LVE maps shown correspond to disc radii  $r = 4^\circ$ ,  $14^\circ$ , and  $50^\circ$ .

Our central findings of the current work are presented in Fig. [8]. In the *top* panel of the figure, we show the amplitude of dipole component underlying the LVE maps estimated for different disc radii as listed in Table 2. Both cases of using a fixed  $N_{\text{side}}=16$  grid and a varying  $N_{\text{side}}$  grid to obtain LVE maps are shown in that figure. The mean and corresponding  $1\sigma$  error from “isotropic” SEVEM FFP12 CMB mocks with noise are shown in *red* colour with square point type and *blue* colour with circle point type for  $N_{\text{side}}=16$  and varying  $N_{\text{side}}$  choices respectively. The dipole amplitude in LVE maps from SEVEM cleaned CMB map from *Planck* 2020 PR4 data set for different disc radii are shown in *red* colour with inverted triangle point type and *blue* colour with a triangle point type for the two cases. One can readily see that the amplitude of the dipole component of LVE maps from data always lies outside the  $1\sigma$  error bars from simulations over a large range of disc radii chosen to compute the LVE maps.

The estimated dipole amplitude from the two cases of fixed  $N_{\text{side}}=16$  and varying  $N_{\text{side}}$  are visibly different, upto  $r \lesssim 40^\circ$  in data. From simulations this difference vanishes for  $r \gtrsim 32^\circ$ . There is an interesting upward turn in the recovered LVE map’s dipole amplitude for  $r = 1^\circ$  in data as well as simulations when using  $N_{\text{side}}=16$  HEALPix grid for estimating LVE maps. Beyond  $r \gtrsim 50^\circ$  (in data), there is no distinction between the mean dipole amplitudes of LVE maps whether one uses fixed  $N_{\text{side}}=16$  or varying  $N_{\text{side}}$  grid to map local variances. For  $r \gtrsim 50^\circ$ , the disc radius chosen is much larger than the LVE map’s  $N_{\text{side}}$  that it makes no difference in the recovered dipole amplitude between the two cases, as is also evident from Table 2.

In the *bottom* panel of Fig. [8], the dipole direction recovered from LVE maps for the same choice of disc radii are shown. The open circles in *red* colour denote dipole directions estimated from LVE maps using fixed  $N_{\text{side}}=16$  and that in *black* colour are same for varying  $N_{\text{side}}$  case. They remarkably span the same region in the sky with nearly overlapping directions. The dipole directions estimated from the data LVE maps with varying  $N_{\text{side}}$  have a similar trend as those from fixed  $N_{\text{side}}=16$  data LVE maps except for few radii. However, we note that collectively they may show a similar trend/span, but when we compare the individual directions recovered for a particular disc radius from the two cases, we find that they are different. One such noticeable difference is the dipole direction for  $r = 1^\circ$  that are  $\sim 50^\circ$  apart as estimated from the two cases. As noted earlier, from the dipole amplitude plot in the top panel, there is also a clear dissimilarity in the estimated magnitudes also for smaller disc radii in generating LVE maps. Also plotted in bottom panel of Fig. [8] is the injected dipole direction [30] as a *green*



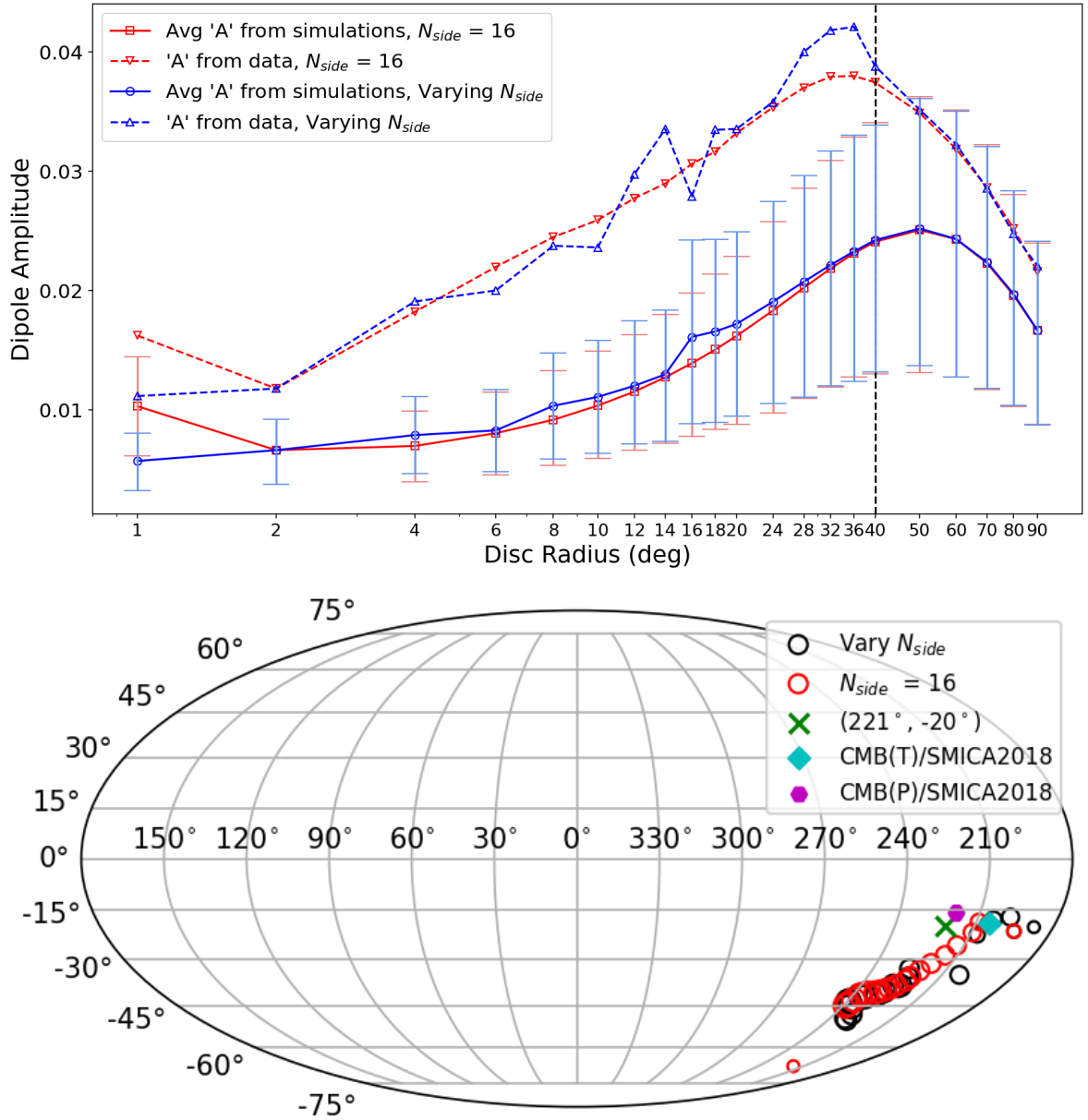


Figure 8: *Top*: Dipole amplitudes from data and mean with  $1\sigma$  errorbars from simulations when using a fixed  $N_{side}=16$  (red - inverted triangle/square) and varying  $N_{side}$  (blue - triangle/circle) to generate normalized variance maps respectively are shown. *Bottom*: Dipole directions extracted from data maps. red and black open circles correspond to fixed  $N_{side}=16$  and varying  $N_{side}$  LVE maps respectively. The data map used here is the SEVEM CMB map from *Planck* PR4 data release. Additionally, the green cross, cyan diamond and purple hexagon points denote the injected dipole direction used in generating the simulations in the present work, LVE dipole from SMICA 2018 CMB temperature map and LVE dipole from SMICA 2018 CMB E-mode polarization map respectively.

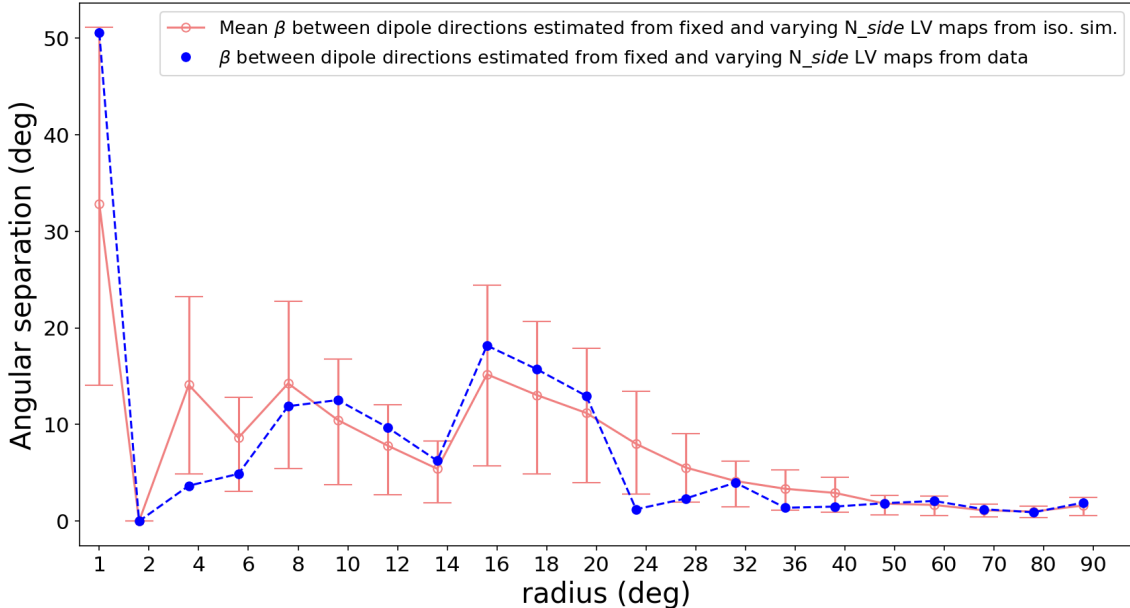


Figure 9: Difference in the dipole direction recovered from LVE maps based on the choice of  $N_{\text{side}}$  used with respect to disc size ‘ $r$ ’.

cross used in the production of modulated maps.

Dipole directions, determined from data LVE maps, are found to differ with the choice of disc radii and  $N_{\text{side}}$  of the pixel grid. The directions so obtained are going away from galactic plane with increase in disc size for both cases. This is evident from the increasing circular point type size used to denote the recovered dipole direction in both cases. However there is an exception for this trend notably for  $r = 1^\circ$  in data LVE map with fixed  $N_{\text{side}}=16$ . In the other case (varying  $N_{\text{side}}$ ) with  $N_{\text{side}}=32$  the trend is consistent as stated, that with increasing disc radius the recovered dipole direction from data LVE maps moves away from the galactic plane. To quantify this difference, let  $\hat{d}$  and  $\hat{e}$  be the dipole directions recovered from data LVE maps using fixed  $N_{\text{side}}=16$  and varying  $N_{\text{side}}$  grids. Then the difference in the recovered dipole directions is given by  $\beta = \cos^{-1}(\hat{d} \cdot \hat{e})$ . The angular separation ‘ $\beta$ ’ (in degrees) in dipole direction for a particular disc radius from data LVE maps prepared with different pixel grid sizes are shown in Fig. [9]. At  $r = 1^\circ$ , the angular separation between the dipole directions in two situations is largest, while for disc radius  $r = 24^\circ$  and beyond they are nearly zero.

The  $p$ -value plot of the dipole amplitudes recovered from data LVE maps for both cases of fixed  $N_{\text{side}}=16$  and varying  $N_{\text{side}}$  are shown in Fig. [10]. Here the  $p$ -values are being calculated in a frequentist manner i.e., as ratio of the number of times dipole amplitude estimated from isotropic simulations exceeding that found in data maps to the total number of (isotropic) simulations used. In Fig. [10] *red* filled circle point types connected by a dashed line correspond to using fixed  $N_{\text{side}}=16$  grid and *black* stars connected by a solid line correspond to varying  $N_{\text{side}}$  grid in obtaining LVE maps. Some of the  $p$ -values are shown encircled by a larger *yellow* open circle. They highlight the disc sizes for which dipole amplitude from local variance maps whose  $p$ -values are zero per the simulation ensemble size used. For large disc radii ( $40^\circ$  onwards) where the choice of  $N_{\text{side}}$  do not make any difference,  $p$ -values are same in both cases. In contrast, at lower disc radii the discrepancy is quite visible. For disc radius  $4^\circ$  to  $10^\circ$  in case of using fixed  $N_{\text{side}}=16$ , number of isotropic simulations (in terms of dipole amplitude evaluated from isotropic LVE maps) exceeding that of data maps is zero implying that their random chance occurrence probability is  $p < 0.0016$  i.e., a more than  $3\sigma$  significance. The analysis with varying  $N_{\text{side}}$  LVE maps gives  $\sim 3\sigma$  significance or less in the range of disc radii  $4^\circ$  to  $14^\circ$ . It is clear from the plot that the analysis results in finding the LVE map dipole amplitudes seen in data

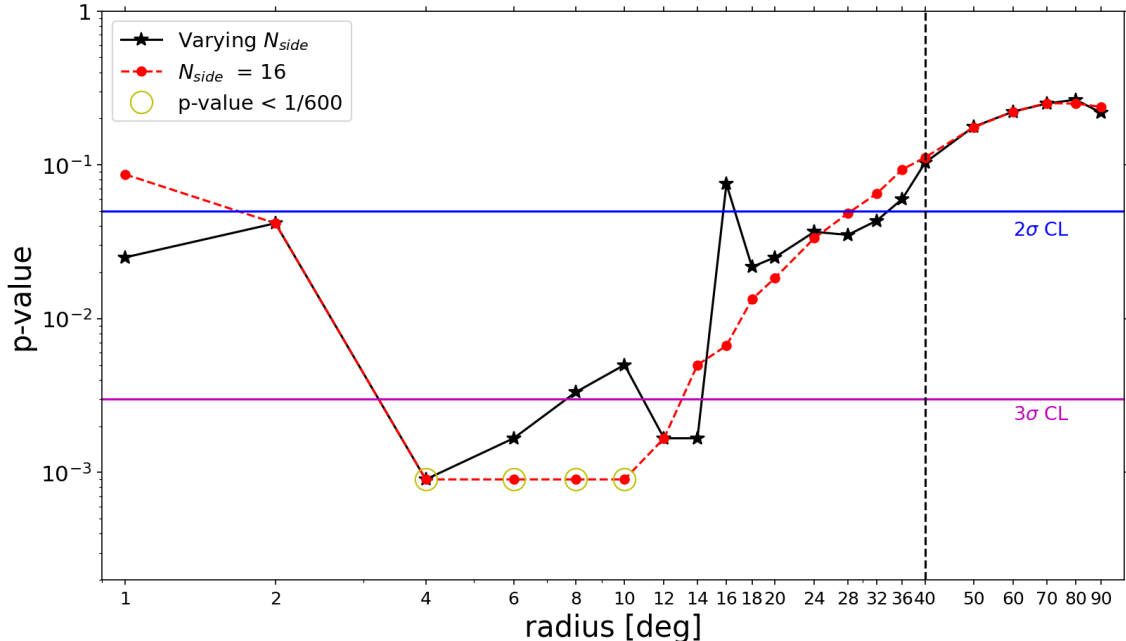


Figure 10:  $p$ -value of the observed dipole amplitude in SEVEM 2020 data maps as a function of disc size ‘ $r$ ’ used to compute LVE maps. Red dots connected by a dashed line and black stars joined by a solid line are used for  $N_{\text{side}}=16$  and varying  $N_{\text{side}}$  cases respectively. A yellow open circle denotes  $p$ -value  $< 1/600$  when there are no simulations whose LVE map’s dipole amplitude exceeds the data value. The two horizontal lines indicate the  $2\sigma$  (blue) and  $3\sigma$  (magenta) significances respectively.

are outside 95% CL with either choice of the LVE map resolution. The case with  $r = 16^\circ$  and  $N_{\text{side}}=2$  is somewhat different, as we do not have the liberty for smooth transitioning of the map resolution as compared to the disc sizes when using HEALPix. From Table 2, the length of diagonal of a pixel grid is  $41^\circ$  for maps having resolution of  $N_{\text{side}}=2$ . If circular discs are circumscribing the square shaped pixel then at least the radius of circular disc be  $20^\circ$  to cover the full pixel information, but with the choice of  $r = 16^\circ$  we are being force to omit some of the pixel information. Instead, if we happen to do the analysis with  $N_{\text{side}}=4$  (diagonal-wise pixel size is  $21^\circ$ ), we found that the  $p$ -value has more than  $2\sigma$  significance.

In Table 3, we summarize our findings viz., the dipole amplitudes, directions, and the corresponding  $p$ -value found for various disc radii chosen to compute LVE maps in the two cases of fixed  $N_{\text{side}}=16$  and varying  $N_{\text{side}}$ . Dipole amplitudes that we recover are biased due to a random dipole component as per Eq. (6) and (7). Following Eq. (8) we obtain the bias corrected dipole amplitudes, where the random dipole power is calculated from the isotropic simulations. The bias corrected dipole amplitude obtained from data maps are presented in Table 3 along with  $1\sigma$  error for different disc radii. Those values that are highlighted in orange colour in Table 3 correspond to the disc radii whose  $p$ -value of the observed dipole amplitude in data LVE maps are outside  $2\sigma$  confidence limit.

## 5 Conclusions

In this paper, we made a reassessment of Hemispherical Power Asymmetry (HPA) seen in CMB temperature data, first in NASA’s WMAP first year CMB maps and then in all its subsequent data releases as well as all the data release from ESA’s *Planck* probe (until PR3). We made use of the SEVEM CMB solution from the final data release (PR4) from *Planck* probe. A set of 600

complementary simulations were provided as part of PR4 corresponding to observed CMB map derived using SEVEM cleaning method. Using the local variance estimation (LVE) method, we probed the hemispherical power asymmetry as dipole modulation of otherwise isotropic CMB sky. We employed a range of disc radii starting from  $1^\circ$  to  $90^\circ$  to map locally computed variances from the CMB sky. These local variances are computed from regions outside the PR3 common mask, recommended for analysis of CMB data from *Planck*'s PR4.

First, we revalidated the method using three sets of simulation ensembles viz., the isotropic CMB realizations with noise from *Planck* PR4 i.e., FFP12 simulation set as given (iso), then dipole modulated CMB maps (pure-dm), and low- $l$  only modulated CMB maps (low- $l$ -dm) that are also added with corresponding FFP12 SEVEM processed noise maps. Our purpose of re-evaluation is to explicitly demonstrate some aspects of the LVE map estimation procedure, specifically, the use of inverse variance weighting to fit the dipole underlying LVE maps, and the correlations that exist between different locally computed variances in LVE maps due to use of overlapping information (pixels) of the CMB sky which is especially relevant when mapping local variances using larger disc radii. We have shown that when using a fixed  $N_{\text{side}}=16$  for LVE maps (whose HEALPix pixel size is  $\sim 4^\circ$ ), some parts of the CMB sky are not used when considering small disc radii such as  $2^\circ$  or less, where as, some regions (pixels of CMB sky) are common to many locally computed variances in an LVE map and consequently (very well) correlated when considering larger disc radii such as  $\sim 32^\circ$  or more.

In order to minimize the correlations in LVE maps to probe HPA, we showed that it can be achieved by matching the  $N_{\text{side}}$  of LVE maps with the disc radii chosen as closely as possible. So instead of using a fixed  $N_{\text{side}}=16$  as originally used [14], we should use a varying  $N_{\text{side}}$  grid for generating LVE maps. Not only did it reduce the correlations in LVE maps, it also fastens the LVE maps' estimation process. Even after matching an LVE map's  $N_{\text{side}}$  with the disc radius used, the variance of an LVE map's pixels are different. So using this information gives an improved fit to the estimation of dipole underlying an LVE map. We note that in our revalidation of LVE method, the difference is negligible when fitting the dipole from LVE maps as they are and using the diagonal elements of the LVE maps' covariance matrix for a particular disc radius from simulations as weights (inverse variance weighting). This could be because of the strong signal to noise ratio in the CMB temperature data. We expect that these choices will be more relevant to CMB polarization data which will be undertaken in a future work.

Some of the observations made during this re-evaluation of LVE method are as follows. The amplitude of the dipole recovered from LVE maps were lower than the injected value for larger disc radii. This is true of both approaches of fixed  $N_{\text{side}}=16$  and varying  $N_{\text{side}}$  to map local variances of a CMB sky, indicating a limitation on the reliability of the LVE method up to only some maximum disc radius. In our study we simulated dipole modulated maps with an amplitude of  $A \approx 0.07$  in the direction  $(\ell, b) = (221^\circ, -20^\circ)$ . With a tolerance level of a 10% deviation of the mean recovered dipole direction from the simulations, but nevertheless consistent with the injected dipole direction in the simulations within errorbars, the LVE method can be used choosing a maximum disc radius of  $\sim 40^\circ$  as demonstrated in Fig. [5]. We also tested the range of validity i.e., the maximum disc radius we can use to apply the LVE method depending on the strength of the underlying anisotropy. We found that for higher levels of dipole modulation amplitude that could be present in a CMB map, the maximum disc radius to use is relatively lower. In any case, for very large disc radius the LVE method breaks down and should not be used.

After this comprehensive re-validation, we applied LVE method with fixed  $N_{\text{side}}=16$  and varying  $N_{\text{side}}$  for different choices of disc radii from  $r = 1^\circ$  to  $90^\circ$ . We used the more appropriate inverse variance weighting method to fit the dipole in LVE maps thus estimated from SEVEM cleaned CMB maps from *Planck* PR4. We find that there is a broad clustering of the dipole directions underlying the observed CMB sky for different disc radii chosen. Nevertheless there is a tendency for these radii to move away from the galactic plane with increasing size of the

Disc Radius ( $r$ )	Fixed $N_{\text{side}}$	$A_{\text{corr}}$	$(\ell, b)$	$p$ -value	Varying $N_{\text{side}}$	$A_{\text{corr}}$	$(\ell, b)$	$p$ -value
1°	16	$0.0118^{+0.0041}_{-0.0042}$	(217°, -67°)	0.0866	32	$0.0093^{+0.0024}_{-0.0025}$	(187°, -20°)	0.0250
2°	16	$0.0093^{+0.0026}_{-0.0028}$	(194°, -22°)	0.0416	16	$0.0093^{+0.0026}_{-0.0028}$	(194°, -22°)	0.0416
4°	16	$0.0166^{+0.0029}_{-0.0030}$	(205°, -20°)	<1/600	8	$0.0171^{+0.0033}_{-0.0032}$	(207°, -23°)	<1/600
6°	16	$0.0202 \pm 0.0035$	(209°, -19°)	<1/600	8	$0.0179 \pm 0.0034$	(204°, -18°)	0.0016
8°	16	$0.0224^{+0.0041}_{-0.0038}$	(210°, -22°)	<1/600	4	$0.0209^{+0.0044}_{-0.0045}$	(198°, -17°)	0.0033
10°	16	$0.0233^{+0.0046}_{-0.0044}$	(213°, -26°)	<1/600	4	$0.0203 \pm 0.0047$	(203°, -35°)	0.0050
12°	16	$0.0248^{+0.0048}_{-0.0049}$	(215°, -29°)	0.0016	4	$0.0267^{+0.0055}_{-0.0049}$	(223°, -36°)	0.0016
14°	16	$0.0255^{+0.0053}_{-0.0056}$	(218°, -31°)	0.0050	4	$0.0304^{+0.0054}_{-0.0056}$	(225°, -33°)	0.0016
16°	16	$0.0266^{+0.0059}_{-0.0061}$	(221°, -34°)	0.0066	2	$0.0216^{+0.0081}_{-0.0073}$	(233°, -49°)	0.0750
18°	16	$0.0271^{+0.0063}_{-0.0067}$	(222°, -36°)	0.0133	2	$0.0281^{+0.0077}_{-0.0076}$	(231°, -50°)	0.0216
20°	16	$0.0281^{+0.0067}_{-0.0074}$	(223°, -37°)	0.0183	2	$0.0277 \pm 0.0077$	(232°, -48°)	0.0250
24°	16	$0.0291^{+0.0075}_{-0.0086}$	(225°, -38°)	0.0333	2	$0.0291^{+0.0084}_{-0.0085}$	(227°, -38°)	0.0366
28°	16	$0.0296^{+0.0083}_{-0.0093}$	(227°, -39°)	0.0483	2	$0.0329^{+0.0089}_{-0.0097}$	(224°, -39°)	0.0350
32°	16	$0.0294^{+0.0091}_{-0.0099}$	(228°, -40°)	0.0650	2	$0.0340^{+0.0095}_{-0.0101}$	(223°, -38°)	0.0433
36°	16	$0.0281^{+0.0097}_{-0.0103}$	(230°, -40°)	0.0933	2	$0.0333^{+0.0097}_{-0.0109}$	(228°, -40°)	0.0600
40°	16	$0.0263^{+0.0100}_{-0.0105}$	(231°, -41°)	0.1116	2	$0.0281^{+0.0097}_{-0.0110}$	(230°, -41°)	0.1033
50°	16	$0.0209^{+0.0112}_{-0.0119}$	(235°, -41°)	0.1750	2	$0.0212^{+0.0109}_{-0.0115}$	(237°, -42°)	0.1766
60°	16	$0.0167^{+0.0108}_{-0.0116}$	(237°, -42°)	0.2216	2	$0.0173^{+0.0107}_{-0.0116}$	(234°, -42°)	0.2216
70°	16	$0.0140^{+0.0099}_{-0.0106}$	(238°, -43°)	0.2516	2	$0.0137^{+0.0097}_{-0.0106}$	(239°, -43°)	0.2500
80°	16	$0.0123^{+0.0085}_{-0.0094}$	(238°, -44°)	0.2500	2	$0.0112^{+0.0087}_{-0.0093}$	(239°, -44°)	0.2650
90°	16	$0.0108^{+0.0073}_{-0.0079}$	(239°, -45°)	0.2383	2	$0.0117^{+0.0074}_{-0.0079}$	(236°, -45°)	0.2183

Table 3: Bias corrected dipole amplitudes underlying LVE maps estimated at different disc radii from SEVEM PR4 CMB map and the corresponding  $p$ -values are shown here. Also presented are the corresponding dipole directions in galactic coordinates  $(\ell, b)$ .



disc radius. We further found that there is a difference in the dipole direction recovered in the two cases, the largest being  $\sim 50^\circ$  for  $r = 1^\circ$ .

The dipole amplitude estimated from the two approaches i.e., fixed  $N_{\text{side}}=16$  and varying  $N_{\text{side}}$  for LVE maps gave slightly different amplitudes, expectedly, and so their  $p$ -values are also different. While with fixed  $N_{\text{side}}=16$  LVE maps, no simulations (out of 600) were found to have a dipole amplitude greater than that seen in data for disc sizes  $r = 4^\circ$  to  $10^\circ$ , with varying  $N_{\text{side}}$  such a situation was seen only for  $r = 4^\circ$  when mapping the local variances using  $N_{\text{side}}=8$ . Further in case of fixed  $N_{\text{side}}=16$  LVE maps, the dipole amplitudes are anomalous at  $2\sigma$  confidence level or more for  $r = 2^\circ$  to  $28^\circ$  disc radii. When employing varying  $N_{\text{side}}$  grid for LVE maps, for disc radius of  $1^\circ$  to  $32^\circ$  (except for  $r = 16^\circ$ ) the estimated dipole amplitudes are anomalous at  $2\sigma$  significance or better.

Thus we confirm earlier findings that there is a significant hemispherical power asymmetry underlying the CMB sky as a dipole modulation field. We also confirm that the dipole direction of HPA is consistent broadly when assessing with different choices of disc radii. Since different modes (angular scales) contribute to estimating variances locally when using different disc sizes, the dipole directions thus recovered could in principle be different. So we are driven to conclude that the HPA direction is robust with respect to different choices of disc radii (or equivalently filter sizes) used to compute LVE maps as reported in earlier studies. Nevertheless the dipole amplitude is different for different disc radii used, implying that we have a scale dependent HPA amplitude. So, the presence of hemispherical power asymmetry in CMB data remains as an open question within the framework of standard cosmological model.

## Acknowledgements

SS acknowledges Ph.D. fellowship received from University Grants Commission (UGC), Inida through UGC-Ref No.:1487/(CSIR-UGC NET JUNE 2018). A.S. would like to acknowledge the support by National Research Foundation of Korea 2021M3F7A1082056, and the support of the Korea Institute for Advanced Study (KIAS) grant funded by the government of Korea. Part of the results presented here are based on observations obtained with *Planck* an ESA science mission with instruments and contributions directly funded by ESA Member States, NASA, and Canada. This research used resources of the National Energy Research Scientific Computing Center (NERSC), a U.S. Department of Energy Office of Science User Facility operated under Contract No. DE-AC02-05CH11231. Further, this work also made use of the following software packages : HEALPix/Healpy [33, 34], SciPy<sup>4</sup> [35], NumPy<sup>5</sup> [36], Astropy<sup>6</sup> [37, 38, 39], and matplotlib<sup>7</sup> [40].

## References

- [1] G. F. Smoot, C. L. Bennett, A. Kogut, J. Aymon, C. Backus, G. de Amici, K. Galuk, P. D. Jackson, P. Keegstra, L. Rokke, L. Tenorio, S. Torres, S. Gulkis, M. G. Hauser, M. Janssen, J. C. Mather, R. Weiss, D. T. Wilkinson, E. L. Wright, N. W. Boggess, E. S. Cheng, T. Kelsall, P. Lubin, S. Meyer, S. H. Moseley, T. L. Murdock, R. A. Shafer, and R. F. Silverberg. First results of the COBE satellite measurement of the anisotropy of the cosmic microwave background radiation. *Advances in Space Research*, 11(2):193–205, January 1991.

---

<sup>4</sup><https://scipy.org>

<sup>5</sup><https://numpy.org>

<sup>6</sup><http://www.astropy.org>

<sup>7</sup><https://matplotlib.org/stable/index.html>

- [2] C. L. Bennett, M. Halpern, G. Hinshaw, N. Jarosik, A. Kogut, M. Limon, S. S. Meyer, L. Page, D. N. Spergel, G. S. Tucker, E. Wollack, E. L. Wright, C. Barnes, M. R. Greason, R. S. Hill, E. Komatsu, M. R. Nolta, N. Odegard, H. V. Peiris, L. Verde, and J. L. Weiland. First-year wilkinson microwave anisotropy probe (wmap)\* observations: Preliminary maps and basic results. *The Astrophysical Journal Supplement Series*, 148(1):1, sep 2003.
- [3] Planck Collaboration, Ade, P. A. R., Aghanim, N., Alves, M. I. R., Armitage-Caplan, C., Arnaud, M., Ashdown, M., Atrio-Barandela, F., Aumont, J., Aussel, H., Baccigalupi, C., Banday, A. J., Barreiro, R. B., Barrena, R., Bartelmann, M., Bartlett, J. G., Bartolo, N., Basak, S., Battaner, E., Battye, R., Benabed, K., Benoît, A., Benoit-Lévy, A., Bernard, J.-P., Bersanelli, M., Bertin-court, B., Bethermin, M., Bielewicz, P., Bikmaev, I., Blanchard, A., Bobin, J., Bock, J. J., Böhringer, H., Bonaldi, A., Bonavera, L., Bond, J. R., Borrill, J., Bouchet, F. R., Boulanger, F., Bourdin, H., Bowyer, J. W., Bridges, M., Brown, M. L., Bucher, M., Burenin, R., Burigana, C., Butler, R. C., Calabrese, E., Cappellini, B., Cardoso, J.-F., Carr, R., Carvalho, P., Casale, M., Castex, G., Catalano, A., Challinor, A., Chamballu, A., Chary, R.-R., Chen, X., Chiang, H. C., Chiang, L.-Y., Chon, G., Christensen, P. R., Churazov, E., Church, S., Clemens, M., Clements, D. L., Colombi, S., Colombo, L. P. L., Combet, C., Comis, B., Couchot, F., Coulais, A., Crill, B. P., Cruz, M., Curto, A., Cuttaia, F., Da Silva, A., Dahle, H., Danese, L., Davies, R. D., Davis, R. J., de Bernardis, P., de Rosa, A., de Zotti, G., Déchelette, T., Delabrouille, J., Delouis, J.-M., Démoclès, J., Désert, F.-X., Dick, J., Dickinson, C., Diego, J. M., Dolag, K., Dole, H., Donzelli, S., Doré, O., Douspis, M., Ducout, A., Dunkley, J., Dupac, X., Efstathiou, G., Elsner, F., Enßlin, T. A., Eriksen, H. K., Fabre, O., Falgarone, E., Falvella, M. C., Fantaye, Y., Fergusson, J., Filliard, C., Finelli, F., Flores-Cacho, I., Foley, S., Forni, O., Fosalba, P., Frailis, M., Fraisse, A. A., Franceschi, E., Freschi, M., Fromenteau, S., Frommert, M., Gaier, T. C., Galeotta, S., Gallegos, J., Galli, S., Gandolfo, B., Ganga, K., Gauthier, C., Génova-Santos, R. T., Ghosh, T., Giard, M., Giardino, G., Gilfanov, M., Girard, D., Giraud-Héraud, Y., Gjerløw, E., González-Nuevo, J., Górski, K. M., Gratton, S., Gregorio, A., Gruppuso, A., Gudmundsson, J. E., Haissinski, J., Hamann, J., Hansen, F. K., Hansen, M., Hanson, D., Harrison, D. L., Heavens, A., Helou, G., Hempel, A., Henrot-Versillé, S., Hernández-Monteagudo, C., Herranz, D., Hildebrandt, S. R., Hivon, E., Ho, S., Hobson, M., Holmes, W. A., Hornstrup, A., Hou, Z., Hovest, W., Huey, G., Huppenberger, K. M., Hurier, G., Ilić, S., Jaffe, A. H., Jaffe, T. R., Jasche, J., Jewell, J., Jones, W. C., Juvela, M., Kalberla, P., Kangaslahti, P., Keihänen, E., Kerp, J., Keskitalo, R., Khamitov, I., Kivi-eri, K., Kim, J., Kisner, T. S., Kneissl, R., Knoche, J., Knox, L., Kunz, M., Kurki-Suonio, H., Lacasa, F., Lagache, G., Lähteenmäki, A., Lamarre, J.-M., Langer, M., Lasenby, A., Lattanzi, M., Laureijs, R. J., Lavabre, A., Lawrence, C. R., Le Jeune, M., Leach, S., Leahy, J. P., Leonardi, R., León-Tavares, J., Leroy, C., Lesgourgues, J., Lewis, A., Li, C., Liddle, A., Liguori, M., Lilje, P. B., Linden-Vørnle, M., Lindholm, V., López-Caniego, M., Lowe, S., Lubin, P. M., Macías-Pérez, J. F., MacTavish, C. J., Maffei, B., Maggio, G., Maino, D., Mandolesi, N., Mangilli, A., Marcos-Caballero, A., Marinucci, D., Maris, M., Marleau, F., Marshall, D. J., Martin, P. G., Martínez-González, E., Masi, S., Massardi, M., Matarrese, S., Matsumura, T., Matthai, F., Maurin, L., Mazzotta, P., McDonald, A., McEwen, J. D., McGehee, P., Mei, S., Meinhold, P. R., Melchiorri, A., Melin, J.-B., Mendes, L., Menegoni, E., Mennella, A., Migliaccio, M., Mikkelsen, K., Millea, M., Miniscalco, R., Mitra, S., Miville-Deschênes, M.-A., Molinari, D., Moneti, A., Montier, L., Morgante, G., Morisset, N., Mortlock, D., Moss, A., Munshi, D., Murphy, J. A., Naselsky, P., Nati, F., Natoli, P., Negrello, M., Nesvadba, N. P. H., Netterfield, C. B., Nørgaard-Nielsen, H. U., North, C., Noviello, F., Novikov, D., Novikov, I., O’Dwyer, I. J., Orioux, F., Osborne, S., O’Sullivan, C., Oxborrow, C. A., Paci, F., Pagano, L., Pajot, F., Paladini, R., Pandolfi, S., Paoletti, D., Partridge, B., Pasian, F., Patanchon, G., Paykari, P., Pearson, D., Pearson, T. J., Peel, M., Peiris, H. V., Perdureau, O., Perotto, L., Perrotta, F., Pettorino, V., Pia-

centini, F., Piat, M., Pierpaoli, E., Pietrobon, D., Plaszczynski, S., Platania, P., Pogosyan, D., Pointecouteau, E., Polenta, G., Ponthieu, N., Popa, L., Poutanen, T., Pratt, G. W., Prézeau, G., Prunet, S., Puget, J.-L., Pullen, A. R., Rachen, J. P., Racine, B., Rahlin, A., Räth, C., Reach, W. T., Rebolo, R., Reinecke, M., Remazeilles, M., Renault, C., Renzi, A., Riazuelo, A., Ricciardi, S., Riller, T., Ringeval, C., Ristorcelli, I., Robbers, G., Rocha, G., Roman, M., Rosset, C., Rossetti, M., Roudier, G., Rowan-Robinson, M., Rubiño-Martín, J. A., Ruiz-Granados, B., Rusholme, B., Salerno, E., Sandri, M., Sanselme, L., Santos, D., Savelainen, M., Savini, G., Schaefer, B. M., Schiavon, F., Scott, D., Seiffert, M. D., Serra, P., Shellard, E. P. S., Smith, K., Smoot, G. F., Souradeep, T., Spencer, L. D., Starck, J.-L., Stolyarov, V., Stompor, R., Sudiwala, R., Sunyaev, R., Sureau, F., Sutter, P., Sutton, D., Suur-Uski, A.-S., Sygnet, J.-F., Tauber, J. A., Tavagnacco, D., Taylor, D., Terenzi, L., Texier, D., Toffolatti, L., Tomasi, M., Torre, J.-P., Tristram, M., Tucci, M., Tuovinen, J., Türler, M., Tuttlebee, M., Umana, G., Valenziano, L., Valiviita, J., Van Tent, B., Varis, J., Vibert, L., Viel, M., Vielva, P., Villa, F., Vittorio, N., Wade, L. A., Wandelt, B. D., Watson, C., Watson, R., Wehus, I. K., Welikala, N., Weller, J., White, M., White, S. D. M., Wilkinson, A., Winkel, B., Xia, J.-Q., Yvon, D., Zacchei, A., Zibin, J. P., and Zonca, A. Planck 2013 results. i. overview of products and scientific results. *A&A*, 571:A1, 2014.

- [4] E Allys, K Arnold, J Aumont, R Aurlien, S Azzoni, C Baccigalupi, A J Banday, R Banerji, R B Barreiro, N Bartolo, L Bautista, D Beck, S Beckman, M Bersanelli, F Boulanger, M Brilenkov, M Bucher, E Calabrese, P Campeti, A Carones, F J Casas, A Catalano, V Chan, K Cheung, Y Chinone, S E Clark, F Columbro, G D’Alessandro, P de Bernardis, T de Haan, E de la Hoz, M De Petris, S Della Torre, P Diego-Palazuelos, M Dobbs, T Dotani, J M Duval, T Elleflot, H K Eriksen, J Errard, T Essinger-Hileman, F Finelli, R Flauger, C Franceschet, U Fuskeland, M Galloway, K Ganga, M Gerbino, M Gervasi, R T Génova-Santos, T Ghigna, S Giardiello, E Gjøløw, J Grain, F Grupp, A Gruppuso, J E Gudmundsson, N W Halverson, P Hargrave, T Hasebe, M Hasegawa, M Hazumi, S Henrot-Versillé, B Hensley, L T Hergt, D Herman, E Hivon, R A Hlozek, A L Hornsby, Y Hoshino, J Hubmayr, K Ichiki, T Iida, H Imada, H Ishino, G Jaehnig, N Katayama, A Kato, R Kesitalo, T Kisner, Y Kobayashi, A Kogut, K Kohri, E Komatsu, K Komatsu, K Konishi, N Krachmalnicoff, C L Kuo, L Lamagna, M Lattanzi, A T Lee, C Leloup, F Levrier, E Linder, G Luzzi, J Macias-Perez, T Maciaszek, B Maffei, D Maino, S Mandelli, E Martínez-González, S Masi, M Massa, S Matarrese, F T Matsuda, T Matsumura, L Mele, M Migliaccio, Y Minami, A Moggi, J Montgomery, L Montier, G Morgante, B Mot, Y Nagano, T Nagasaki, R Nagata, R Nakano, T Namikawa, F Nati, P Natoli, S Nerval, F Noviello, K Odagiri, S Oguri, H Ohsaki, L Pagano, A Paiella, D Paoletti, A Passerini, G Patanchon, F Piacentini, M Piat, G Pisano, G Polenta, D Poletti, T Prouvé, G Puglisi, D Rambaud, C Raum, S Realini, M Reinecke, M Remazeilles, A Ritacco, G Roudil, J A Rubino-Martin, M Russell, H Sakurai, Y Sakurai, M Sasaki, D Scott, Y Sekimoto, K Shinozaki, M Shiraishi, P Shirron, G Signorelli, F Spinella, S Stever, R Stompor, S Sugiyama, R M Sullivan, A Suzuki, T L Svalheim, E Switzer, R Takaku, H Takakura, Y Takase, A Tartari, Y Terao, J Thermeau, H Thommesen, K L Thompson, M Tomasi, M Tominaga, M Tristram, M Tsuji, M Tsujimoto, L Vacher, P Vielva, N Vittorio, W Wang, K Watanuki, I K Wehus, J Weller, B Westbrook, J Wilms, B Winter, E J Wollack, J Yumoto, and M Zannoni. Probing cosmic inflation with the litebird cosmic microwave background polarization survey. *Progress of Theoretical and Experimental Physics*, 2023(4), November 2022.
- [5] Shaul Hanany, Marcelo Alvarez, Emmanuel Artis, Peter Ashton, Jonathan Aumont, Ragnhild Aurlien, Ranajoy Banerji, R. Belen Barreiro, James G. Bartlett, Soumen Basak, Nick Battaglia, Jamie Bock, Kimberly K. Boddy, Matteo Bonato, Julian Borrill, François Bouchet, François Boulanger, Blakesley Burkhart, Jens Chluba, David Chuss, Susan E. Clark, Joelle Cooper, Brendan P. Crill, Gianfranco De Zotti, Jacques Delabrouille,

- Eleonora Di Valentino, Joy Didier, Olivier Doré, Hans K. Eriksen, Josquin Errard, Tom Essinger-Hileman, Stephen Feeney, Jeffrey Filippini, Laura Fissel, Raphael Flauger, Unni Fuskeland, Vera Gluscevic, Krzysztof M. Gorski, Dan Green, Shaul Hanany, Brandon Hensley, Diego Herranz, J. Colin Hill, Eric Hivon, Renée Hložek, Johannes Hubmayr, Bradley R. Johnson, William Jones, Terry Jones, Lloyd Knox, Al Kogut, Marcos López-Caniego, Charles Lawrence, Alex Lazarian, Zack Li, Mathew Madhavacheril, Jean-Baptiste Melin, Joel Meyers, Calum Murray, Mattia Negrello, Giles Novak, Roger O’Brient, Christopher Paine, Tim Pearson, Levon Pogosian, Clem Pryke, Giuseppe Puglisi, Mathieu Remazeilles, Graca Rocha, Marcel Schmittfull, Douglas Scott, Peter Shirron, Ian Stephens, Brian Sutin, Maurizio Tomasi, Amy Trangsud, Alexander van Engelen, Flavien Vansyngel, Ingunn K. Wehus, Qi Wen, Siyao Xu, Karl Young, and Andrea Zonca. PICO: Probe of Inflation and Cosmic Origins. In *Bulletin of the American Astronomical Society*, volume 51, page 194, September 2019.
- [6] Debabrata Adak, Aparajita Sen, Soumen Basak, Jacques Delabrouille, Tuhin Ghosh, Aditya Rotti, Ginés Martínez-Solaèche, and Tarun Souradeep. B-mode forecast of cmb-bhārat. *Monthly Notices of the Royal Astronomical Society*, 514(2):3002–3016, May 2022.
- [7] A. Kogut, D.J. Fixsen, D.T. Chuss, J. Dotson, E. Dwek, M. Halpern, G.F. Hinshaw, S.M. Meyer, S.H. Moseley, M.D. Seiffert, D.N. Spergel, and E.J. Wollack. The primordial inflation explorer (pixie): a nulling polarimeter for cosmic microwave background observations. *Journal of Cosmology and Astroparticle Physics*, 2011(07):025–025, July 2011.
- [8] H. K. Eriksen, F. K. Hansen, A. J. Banday, K. M. Gorski, and P. B. Lilje. Asymmetries in the cosmic microwave background anisotropy field. *The Astrophysical Journal*, 605(1):14–20, April 2004.
- [9] H. K. Eriksen, A. J. Banday, K. M. Górski, F. K. Hansen, and P. B. Lilje. Hemispherical power asymmetry in the third-year wilkinson microwave anisotropy probe sky maps. *The Astrophysical Journal*, 660(2):L81–L84, April 2007.
- [10] F. K. Hansen, A. J. Banday, and K. M. Górski. Testing the cosmological principle of isotropy: local power-spectrum estimates of the wmap data. *Monthly Notices of the Royal Astronomical Society*, 354(3):641–665, November 2004.
- [11] Amir Hajian, Tarun Souradeep, and Neil Cornish. Statistical Isotropy of the Wilkinson Microwave Anisotropy Probe Data: A Bipolar Power Spectrum Analysis. *ApJ*, 618(2):L63–L66, January 2005.
- [12] F. Paci, A. Gruppuso, F. Finelli, P. Cabella, A. De Rosa, N. Mandolesi, and P. Natoli. Power asymmetries in the cosmic microwave background temperature and polarization patterns. *Monthly Notices of the Royal Astronomical Society*, 407(1):399–404, 08 2010.
- [13] Pranati K. Rath and Pankaj Jain. Testing the dipole modulation model in cmb. *Journal of Cosmology and Astroparticle Physics*, 2013(12):014, dec 2013.
- [14] Y. Akrami, Y. Fantaye, A. Shafieloo, H. K. Eriksen, F. K. Hansen, A. J. Banday, and K. M. Górski. Power Asymmetry in WMAP and Planck Temperature Sky Maps as Measured by a Local Variance Estimator. *ApJ*, 784(2):L42, April 2014.
- [15] Simone Aiola, Bingjie Wang, Arthur Kosowsky, Tina Kahniashvili, and Hassan Firouzjahi. Microwave background correlations from dipole anisotropy modulation. *Physical Review D*, 92(6), September 2015.

- [16] Shamik Ghosh, Rahul Kothari, Pankaj Jain, and Pranati K. Rath. Dipole modulation of cosmic microwave background temperature and polarization. *Journal of Cosmology and Astroparticle Physics*, 2016(01):046–046, January 2016.
- [17] Shabbir Shaikh, Suvodip Mukherjee, Santanu Das, Benjamin D. Wandelt, and Tarun Souradeep. Joint Bayesian analysis of large angular scale CMB temperature anomalies. *J. Cosmology Astropart. Phys.*, 2019(8):007, August 2019.
- [18] C. Gimeno-Amo, R.B. Barreiro, E. Martínez-González, and A. Marcos-Caballero. Hemispherical power asymmetry in intensity and polarization for planck pr4 data. *Journal of Cosmology and Astroparticle Physics*, 2023(12):029, December 2023.
- [19] M. Axelsson, Y. Fantaye, F. K. Hansen, A. J. Banday, H. K. Eriksen, and K. M. Gorski. Directional Dependence of  $\Lambda$ CDM Cosmological Parameters. *ApJ*, 773(1):L3, August 2013.
- [20] Suvodip Mukherjee, Pavan K. Aluri, Santanu Das, Shabbir Shaikh, and Tarun Souradeep. Direction dependence of cosmological parameters due to cosmic hemispherical asymmetry. *J. Cosmology Astropart. Phys.*, 2016(6):042, June 2016.
- [21] S. Yeung and M. C. Chu. Directional variations of cosmological parameters from the Planck CMB data. *Phys. Rev. D*, 105(8):083508, April 2022.
- [22] John P. Ralston and Pankaj Jain. The Virgo Alignment Puzzle in Propagation of Radiation on Cosmological Scales. *International Journal of Modern Physics D*, 13(9):1857–1877, January 2004.
- [23] Ashok K. Singal. Large Peculiar Motion of the Solar System from the Dipole Anisotropy in Sky Brightness due to Distant Radio Sources. *ApJ*, 742(2):L23, December 2011.
- [24] V. Pelgrims and D. Hutsemékers. Evidence for the alignment of quasar radio polarizations with large quasar group axes. *A&A*, 590:A53, May 2016.
- [25] Nathan J. Secrest, Sebastian von Hausegger, Mohamed Rameez, Roya Mohayaee, Subir Sarkar, and Jacques Colin. A Test of the Cosmological Principle with Quasars. *ApJ*, 908(2):L51, February 2021.
- [26] Jacques Colin, Roya Mohayaee, Mohamed Rameez, and Subir Sarkar. Evidence for anisotropy of cosmic acceleration. *A&A*, 631:L13, November 2019.
- [27] Christopher Gordon, Wayne Hu, Dragan Huterer, and Tom Crawford. Spontaneous isotropy breaking: A mechanism for cmb multipole alignments. *Phys. Rev. D*, 72:103002, Nov 2005.
- [28] R. Fernández-Cobos, P. Vielva, R. B. Barreiro, and E. Martínez-González. Multiresolution internal template cleaning: an application to the Wilkinson Microwave Anisotropy Probe 7-yr polarization data. *MNRAS*, 420(3):2162–2169, March 2012.
- [29] Planck Collaboration, Akrami, Y., Ashdown, M., Aumont, J., Baccigalupi, C., Ballardini, M., Banday, A. J., Barreiro, R. B., Bartolo, N., Basak, S., Benabed, K., Bersanelli, M., Bielewicz, P., Bond, J. R., Borrill, J., Bouchet, F. R., Boulanger, F., Bucher, M., Burigana, C., Calabrese, E., Cardoso, J.-F., Carron, J., Casaponsa, B., Challinor, A., Colombo, L. P. L., Combet, C., Crill, B. P., Cuttaia, F., de Bernardis, P., de Rosa, A., de Zotti, G., Delabrouille, J., Delouis, J.-M., Di Valentino, E., Dickinson, C., Diego, J. M., Donzelli, S., Doré, O., Ducout, A., Dupac, X., Efstathiou, G., Elsner, F., Enßlin, T. A., Eriksen, H. K., Falgarone, E., Fernandez-Cobos, R., Finelli, F., Forastieri, F., Frailis, M., Fraisse, A. A., Franceschi, E., Frolov, A., Galeotta, S., Galli, S., Ganga, K., Génova-Santos, R. T.,



Gerbino, M., Ghosh, T., González-Nuevo, J., Górski, K. M., Gratton, S., Gruppuso, A., Gudmundsson, J. E., Handley, W., Hansen, F. K., Helou, G., Herranz, D., Hildebrandt, S. R., Huang, Z., Jaffe, A. H., Karakci, A., Keihänen, E., Keskitalo, R., Kiiveri, K., Kim, J., Kisner, T. S., Krachmalnicoff, N., Kunz, M., Kurki-Suonio, H., Lagache, G., Lamarre, J.-M., Lasenby, A., Lattanzi, M., Lawrence, C. R., Le Jeune, M., Levrier, F., Liguori, M., Lilje, P. B., Lindholm, V., López-Caniego, M., Lubin, P. M., Ma, Y.-Z., Macías-Pérez, J. F., Maggio, G., Maino, D., Mandolesi, N., Mangilli, A., Marcos-Caballero, A., Maris, M., Martin, P. G., Martínez-González, E., Matarrese, S., Mauri, N., McEwen, J. D., Meinhold, P. R., Melchiorri, A., Mennella, A., Migliaccio, M., Miville-Deschênes, M.-A., Molinari, D., Moneti, A., Montier, L., Morgante, G., Natoli, P., Oppizzi, F., Pagano, L., Paoletti, D., Partridge, B., Peel, M., Pettorino, V., Piacentini, F., Polenta, G., Puget, J.-L., Rachen, J. P., Reinecke, M., Remazeilles, M., Renzi, A., Rocha, G., Roudier, G., Rubiño-Martín, J. A., Ruiz-Granados, B., Salvati, L., Sandri, M., Savelainen, M., Scott, D., Seljebotn, D. S., Sirignano, C., Spencer, L. D., Suur-Uski, A.-S., Tauber, J. A., Tavagnacco, D., Tenti, M., Thommesen, H., Toffolatti, L., Tomasi, M., Trombetti, T., Valiviita, J., Van Tent, B., Vielva, P., Villa, F., Vittorio, N., Wandelt, B. D., Wehus, I. K., Zacchei, A., and Zonca, A. Planck 2018 results - iv. diffuse component separation. *A&A*, 641:A4, 2020.

- [30] Planck Collaboration, Akrami, Y., Ashdown, M., Aumont, J., Baccigalupi, C., Ballardini, M., Banday, A. J., Barreiro, R. B., Bartolo, N., Basak, S., Benabed, K., Bersanelli, M., Bielewicz, P., Bock, J. J., Bond, J. R., Borrill, J., Bouchet, F. R., Boulanger, F., Bucher, M., Burigana, C., Butler, R. C., Calabrese, E., Cardoso, J.-F., Casaponsa, B., Chiang, H. C., Colombo, L. P. L., Combet, C., Contreras, D., Crill, B. P., de Bernardis, P., de Zotti, G., Delabrouille, J., Delouis, J.-M., Di Valentino, E., Diego, J. M., Doré, O., Douspis, M., Ducout, A., Dupac, X., Efstathiou, G., Elsner, F., Enßlin, T. A., Eriksen, H. K., Fantaye, Y., Fernandez-Cobos, R., Finelli, F., Frailis, M., Fraisse, A. A., Franceschi, E., Frolov, A., Galeotta, S., Galli, S., Ganga, K., Génova-Santos, R. T., Gerbino, M., Ghosh, T., González-Nuevo, J., Górski, K. M., Gruppuso, A., Gudmundsson, J. E., Hamann, J., Handley, W., Hansen, F. K., Herranz, D., Hivon, E., Huang, Z., Jaffe, A. H., Jones, W. C., Keihänen, E., Keskitalo, R., Kiiveri, K., Kim, J., Krachmalnicoff, N., Kunz, M., Kurki-Suonio, H., Lagache, G., Lamarre, J.-M., Lasenby, A., Lattanzi, M., Lawrence, C. R., Le Jeune, M., Levrier, F., Liguori, M., Lilje, P. B., Lindholm, V., López-Caniego, M., Ma, Y.-Z., Macías-Pérez, J. F., Maggio, G., Maino, D., Mandolesi, N., Mangilli, A., Marcos-Caballero, A., Maris, M., Martin, P. G., Martínez-González, E., Matarrese, S., Mauri, N., McEwen, J. D., Meinhold, P. R., Mennella, A., Migliaccio, M., Miville-Deschênes, M.-A., Molinari, D., Moneti, A., Montier, L., Morgante, G., Moss, A., Natoli, P., Pagano, L., Paoletti, D., Partridge, B., Perrotta, F., Pettorino, V., Piacentini, F., Polenta, G., Puget, J.-L., Rachen, J. P., Reinecke, M., Remazeilles, M., Renzi, A., Rocha, G., Rosset, C., Roudier, G., Rubiño-Martín, J. A., Ruiz-Granados, B., Salvati, L., Savelainen, M., Scott, D., Shellard, E. P. S., Sirignano, C., Sunyaev, R., Suur-Uski, A.-S., Tauber, J. A., Tavagnacco, D., Tenti, M., Toffolatti, L., Tomasi, M., Trombetti, T., Valenziano, L., Valiviita, J., Van Tent, B., Vielva, P., Villa, F., Vittorio, N., Wandelt, B. D., Wehus, I. K., Zacchei, A., Zibin, J. P., and Zonca, A. Planck 2018 results - vii. isotropy and statistics of the cmb. *A&A*, 641:A7, 2020.
- [31] J. Hoftuft, H. K. Eriksen, A. J. Banday, K. M. Górski, F. K. Hansen, and P. B. Lilje. Increasing evidence for hemispherical power asymmetry in the five-year wmap data. *The Astrophysical Journal*, 699(2):985, jun 2009.
- [32] Saroj Adhikari. Local variance asymmetries in Planck temperature anisotropy maps. *MNRAS*, 446(4):4232–4238, February 2015.

- [33] K. M. Górski, E. Hivon, A. J. Banday, B. D. Wandelt, F. K. Hansen, M. Reinecke, and M. Bartelmann. HEALPix: A Framework for High-Resolution Discretization and Fast Analysis of Data Distributed on the Sphere. *ApJ*, 622(2):759–771, April 2005.
- [34] Andrea Zonca, Leo Singer, Daniel Lenz, Martin Reinecke, Cyrille Rosset, Eric Hivon, and Krzysztof Gorski. healpy: equal area pixelization and spherical harmonics transforms for data on the sphere in python. *Journal of Open Source Software*, 4(35):1298, March 2019.
- [35] Pauli Virtanen, Ralf Gommers, Travis E. Oliphant, Matt Haberland, Tyler Reddy, David Cournapeau, Evgeni Burovski, Pearu Peterson, Warren Weckesser, Jonathan Bright, Stéfan J. van der Walt, Matthew Brett, Joshua Wilson, K. Jarrod Millman, Nikolay Mayorov, Andrew R. J. Nelson, Eric Jones, Robert Kern, Eric Larson, C J Carey, İlhan Polat, Yu Feng, Eric W. Moore, Jake VanderPlas, Denis Laxalde, Josef Perktold, Robert Cimrman, Ian Henriksen, E. A. Quintero, Charles R. Harris, Anne M. Archibald, Antônio H. Ribeiro, Fabian Pedregosa, Paul van Mulbregt, and SciPy 1.0 Contributors. SciPy 1.0: Fundamental Algorithms for Scientific Computing in Python. *Nature Methods*, 17:261–272, 2020.
- [36] Charles R. Harris, K. Jarrod Millman, Stéfan J. van der Walt, Ralf Gommers, Pauli Virtanen, David Cournapeau, Eric Wieser, Julian Taylor, Sebastian Berg, Nathaniel J. Smith, Robert Kern, Matti Picus, Stephan Hoyer, Marten H. van Kerkwijk, Matthew Brett, Allan Haldane, Jaime Fernández del Río, Mark Wiebe, Pearu Peterson, Pierre Gérard-Marchant, Kevin Sheppard, Tyler Reddy, Warren Weckesser, Hameer Abbasi, Christoph Gohlke, and Travis E. Oliphant. Array programming with NumPy. *Nature*, 585(7825):357–362, September 2020.
- [37] Astropy Collaboration, T. P. Robitaille, E. J. Tollerud, P. Greenfield, M. Droettboom, E. Bray, T. Aldcroft, M. Davis, A. Ginsburg, A. M. Price-Whelan, W. E. Kerzendorf, A. Conley, N. Crighton, K. Barbary, D. Muna, H. Ferguson, F. Grollier, M. M. Parikh, P. H. Nair, H. M. Unther, C. Deil, J. Woillez, S. Conseil, R. Kramer, J. E. H. Turner, L. Singer, R. Fox, B. A. Weaver, V. Zabalza, Z. I. Edwards, K. Azalee Bostroem, D. J. Burke, A. R. Casey, S. M. Crawford, N. Dencheva, J. Ely, T. Jenness, K. Labrie, P. L. Lim, F. Pierfederici, A. Pontzen, A. Ptak, B. Refsdal, M. Servillat, and O. Streicher. Astropy: A community Python package for astronomy. *A&A*, 558:A33, October 2013.
- [38] Astropy Collaboration, A. M. Price-Whelan, B. M. Sipócz, H. M. Günther, P. L. Lim, S. M. Crawford, S. Conseil, D. L. Shupe, M. W. Craig, N. Dencheva, A. Ginsburg, J. T. VanderPlas, L. D. Bradley, D. Pérez-Suárez, M. de Val-Borro, T. L. Aldcroft, K. L. Cruz, T. P. Robitaille, E. J. Tollerud, C. Ardelean, T. Babej, Y. P. Bach, M. Bachetti, A. V. Bakanov, S. P. Bamford, G. Barentsen, P. Barmby, A. Baumbach, K. L. Berry, F. Biscani, M. Boquien, K. A. Bostroem, L. G. Bouma, G. B. Brammer, E. M. Bray, H. Breytenbach, H. Buddelmeijer, D. J. Burke, G. Calderone, J. L. Cano Rodríguez, M. Cara, J. V. M. Cardoso, S. Cheedella, Y. Copin, L. Corrales, D. Crichton, D. D’Avella, C. Deil, É. Depagne, J. P. Dietrich, A. Donath, M. Droettboom, N. Earl, T. Erben, S. Fabbro, L. A. Ferreira, T. Finethy, R. T. Fox, L. H. Garrison, S. L. J. Gibbons, D. A. Goldstein, R. Gommers, J. P. Greco, P. Greenfield, A. M. Groener, F. Grollier, A. Hagen, P. Hirst, D. Homeier, A. J. Horton, G. Hosseinzadeh, L. Hu, J. S. Hunkeler, Ž. Ivezić, A. Jain, T. Jenness, G. Kanarek, S. Kendrew, N. S. Kern, W. E. Kerzendorf, A. Khvalko, J. King, D. Kirkby, A. M. Kulkarni, A. Kumar, A. Lee, D. Lenz, S. P. Littlefair, Z. Ma, D. M. Macleod, M. Mastropietro, C. McCully, S. Montagnac, B. M. Morris, M. Mueller, S. J. Mumford, D. Muna, N. A. Murphy, S. Nelson, G. H. Nguyen, J. P. Ninan, M. Nöthe, S. Ogaz, S. Oh, J. K. Parejko, N. Parley, S. Pascual, R. Patil, A. A. Patil, A. L. Plunkett, J. X. Prochaska, T. Rastogi, V. Reddy Janga, J. Sabater, P. Sakurikar, M. Seifert, L. E. Sherbert, H. Sherwood-Taylor,

A. Y. Shih, J. Sick, M. T. Silbiger, S. Singanamalla, L. P. Singer, P. H. Sladen, K. A. Sooley, S. Sornarajah, O. Streicher, P. Teuben, S. W. Thomas, G. R. Tremblay, J. E. H. Turner, V. Terrón, M. H. van Kerkwijk, A. de la Vega, L. L. Watkins, B. A. Weaver, J. B. Whitmore, J. Woillez, V. Zabalza, and Astropy Contributors. The Astropy Project: Building an Open-science Project and Status of the v2.0 Core Package. *AJ*, 156(3):123, September 2018.

- [39] Astropy Collaboration, Adrian M. Price-Whelan, Pey Lian Lim, Nicholas Earl, Nathaniel Starkman, Larry Bradley, David L. Shupe, Aarya A. Patil, Lia Corrales, C. E. Brasseur, Maximilian N’othe, Axel Donath, Erik Tollerud, Brett M. Morris, Adam Ginsburg, Eero Vaher, Benjamin A. Weaver, James Tocknell, William Jamieson, Marten H. van Kerkwijk, Thomas P. Robitaille, Bruce Merry, Matteo Bachetti, H. Moritz G’unther, Thomas L. Aldcroft, Jaime A. Alvarado-Montes, Anne M. Archibald, Attila B’odi, Shreyas Bapat, Geert Barentsen, Juanjo Baz’an, Manish Biswas, M’ed’eric Boquien, D. J. Burke, Daria Cara, Mihai Cara, Kyle E. Conroy, Simon Conseil, Matthew W. Craig, Robert M. Cross, Kelle L. Cruz, Francesco D’Eugenio, Nadia Dencheva, Hadrien A. R. Devillepoix, J’org P. Dietrich, Arthur Davis Eigenbrot, Thomas Erben, Leonardo Ferreira, Daniel Foreman-Mackey, Ryan Fox, Nabil Freij, Suyog Garg, Robel Geda, Lauren Glattly, Yash Gondhalekar, Karl D. Gordon, David Grant, Perry Greenfield, Austen M. Groener, Steve Guest, Sebastian Gurovich, Rasmus Handberg, Akeem Hart, Zac Hatfield-Dodds, Derek Homeier, Griffin Hosseinzadeh, Tim Jenness, Craig K. Jones, Prajwel Joseph, J. Bryce Kalmbach, Emir Karamehmetoglu, Mikolaj Kaluszy’nski, Michael S. P. Kelley, Nicholas Kern, Wolfgang E. Kerzendorf, Eric W. Koch, Shankar Kulumani, Antony Lee, Chun Ly, Zhiyuan Ma, Conor MacBride, Jakob M. Maljaars, Demitri Muna, N. A. Murphy, Henrik Norman, Richard O’Steen, Kyle A. Oman, Camilla Pacifici, Sergio Pascual, J. Pascual-Granado, Rohit R. Patil, Gabriel I. Perren, Timothy E. Pickering, Tanuj Rastogi, Benjamin R. Roulston, Daniel F. Ryan, Eli S. Rykoff, Jose Sabater, Parikshit Sakurikar, Jes’us Salgado, Aniket Sanghi, Nicholas Saunders, Volodymyr Savchenko, Ludwig Schwardt, Michael Seifert-Eckert, Albert Y. Shih, Anany Shrey Jain, Gyanendra Shukla, Jonathan Sick, Chris Simpson, Sudheesh Singanamalla, Leo P. Singer, Jaladh Singhal, Manodeep Sinha, Brigitta M. SipHocz, Lee R. Spitler, David Stansby, Ole Streicher, Jani Šumak, John D. Swinbank, Dan S. Taranu, Nikita Tewary, Grant R. Tremblay, Miguel de Val-Borro, Samuel J. Van Kooten, Zlatan Vasovi’c, Shresth Verma, Jos’e Vin’icius de Miranda Cardoso, Peter K. G. Williams, Tom J. Wilson, Benjamin Winkel, W. M. Wood-Vasey, Rui Xue, Peter Yoachim, Chen Zhang, Andrea Zonca, and Astropy Project Contributors. The Astropy Project: Sustaining and Growing a Community-oriented Open-source Project and the Latest Major Release (v5.0) of the Core Package. *apj*, 935(2):167, August 2022.

- [40] J. D. Hunter. Matplotlib: A 2d graphics environment. *Computing in Science & Engineering*, 9(3):90–95, 2007.

## A LVE maps’ dipole estimation with simple and inverse variance weighting schemes

Here we dwell on few details regarding estimation of dipole underlying normalized local variance maps that were commented about in earlier works, though not explicitly demonstrated.

We use the `remove_dipole` functionality of `HEALPix` as it is to estimate dipole from normalized LVE maps from data or simulations which we call as *simple fit*. When using a mask, depending on the number of pixels available at a specific location at which disc centers are defined to compute local variances, the variance of local variances computed will differ. Further the variances themselves follow a  $\chi^2$  distribution as the CMB temperature anisotropies are

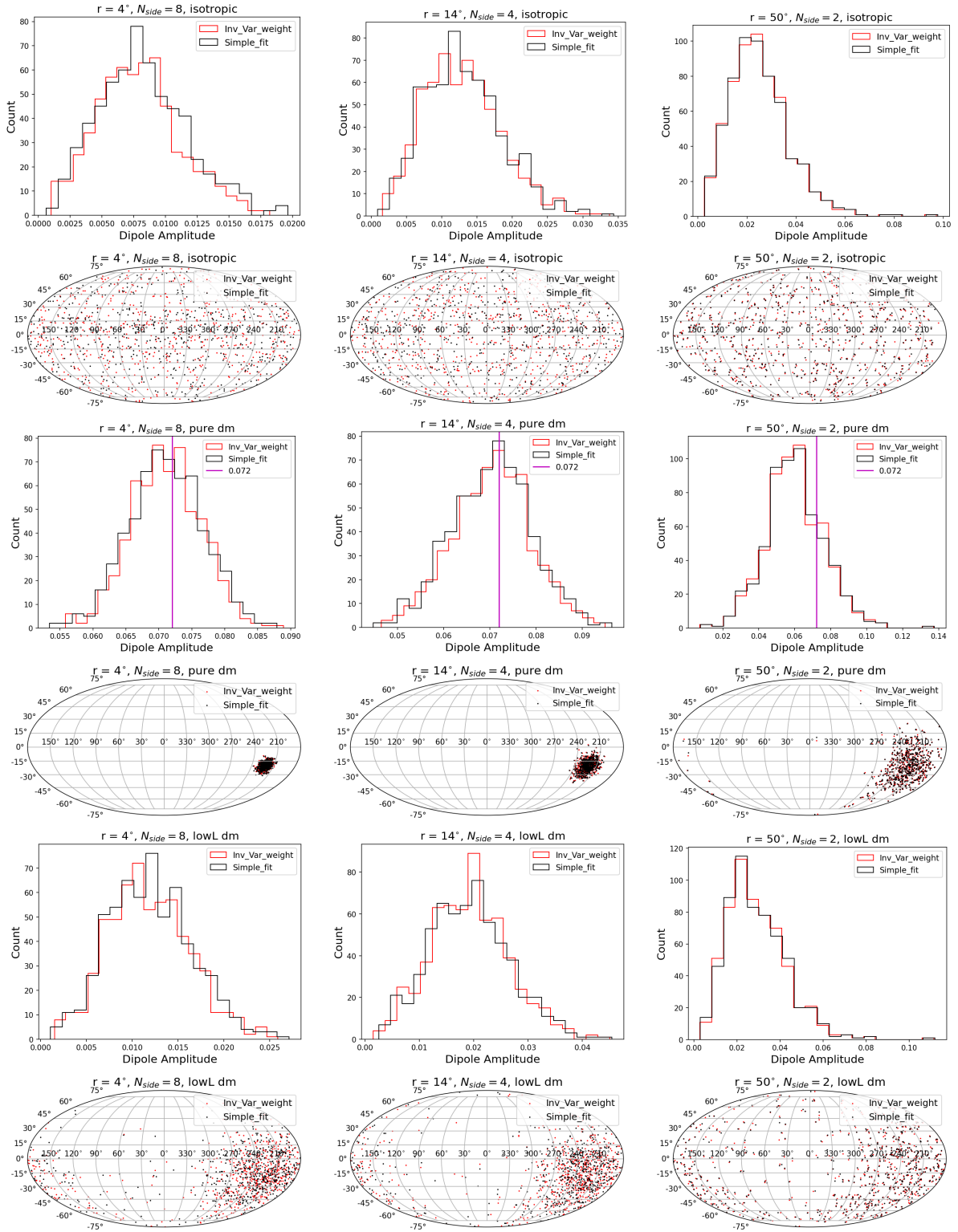


Figure A.1: For some select disc radii  $r = 4^\circ$ ,  $14^\circ$  and  $50^\circ$ , distribution of recovered dipole amplitude and direction are shown when using a simple fit (in *black*) and inverse variance weighting (in *red*) schemes, where varying  $N_{\text{side}}$  grid is used in deriving LVE maps. The *first* and *second* rows correspond to results from isotropic simulation set, *third* and *fourth* correspond to results from pure dipole modulated (dm) simulations, and finally the *fifth* and *sixth* correspond to recovered dipole amplitude and direction respectively from low- $l$  only modulated simulations.

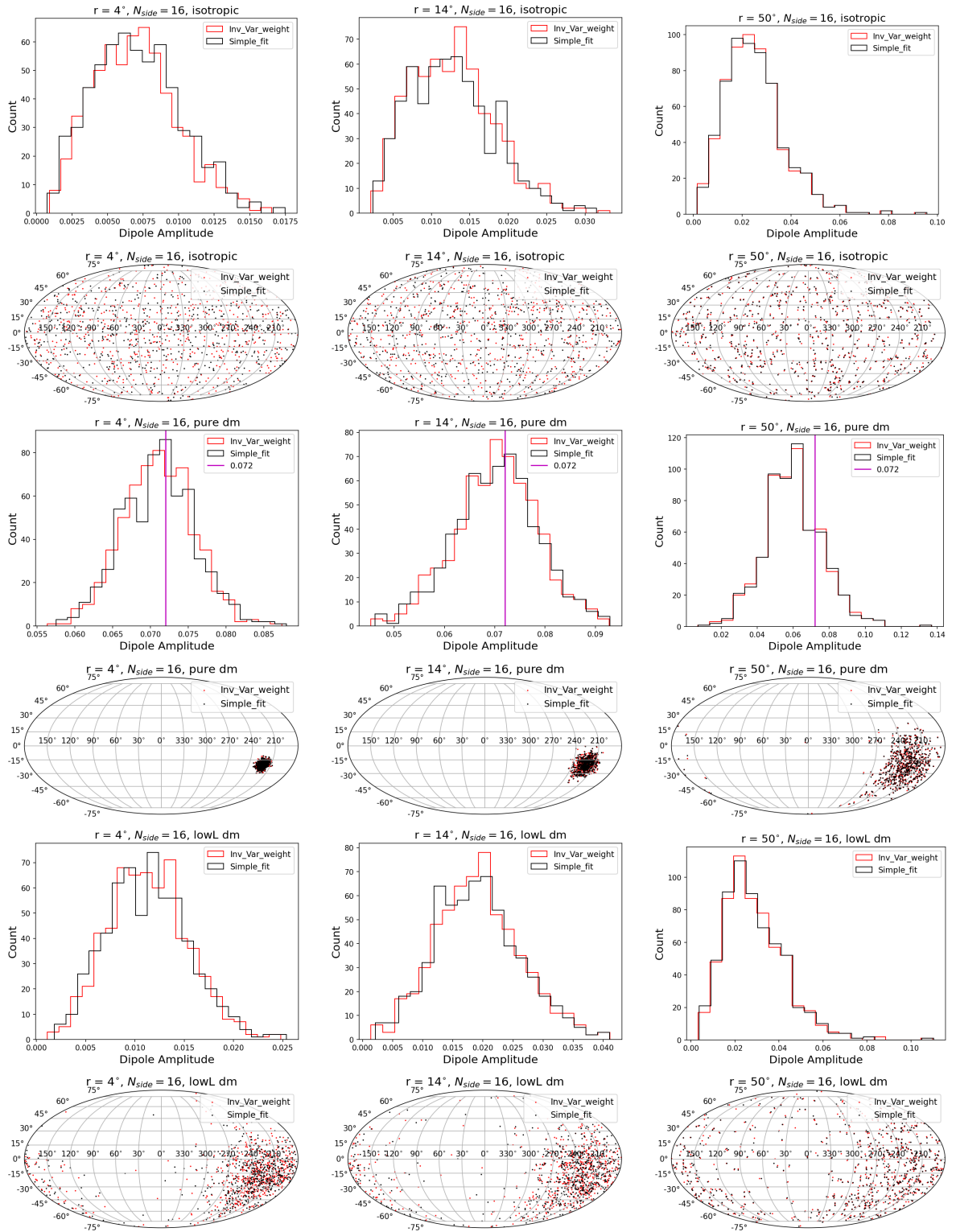


Figure A.2: Same as Fig. [A.1], but when using fixed  $N_{\text{side}}$  grid in deriving LVE maps.

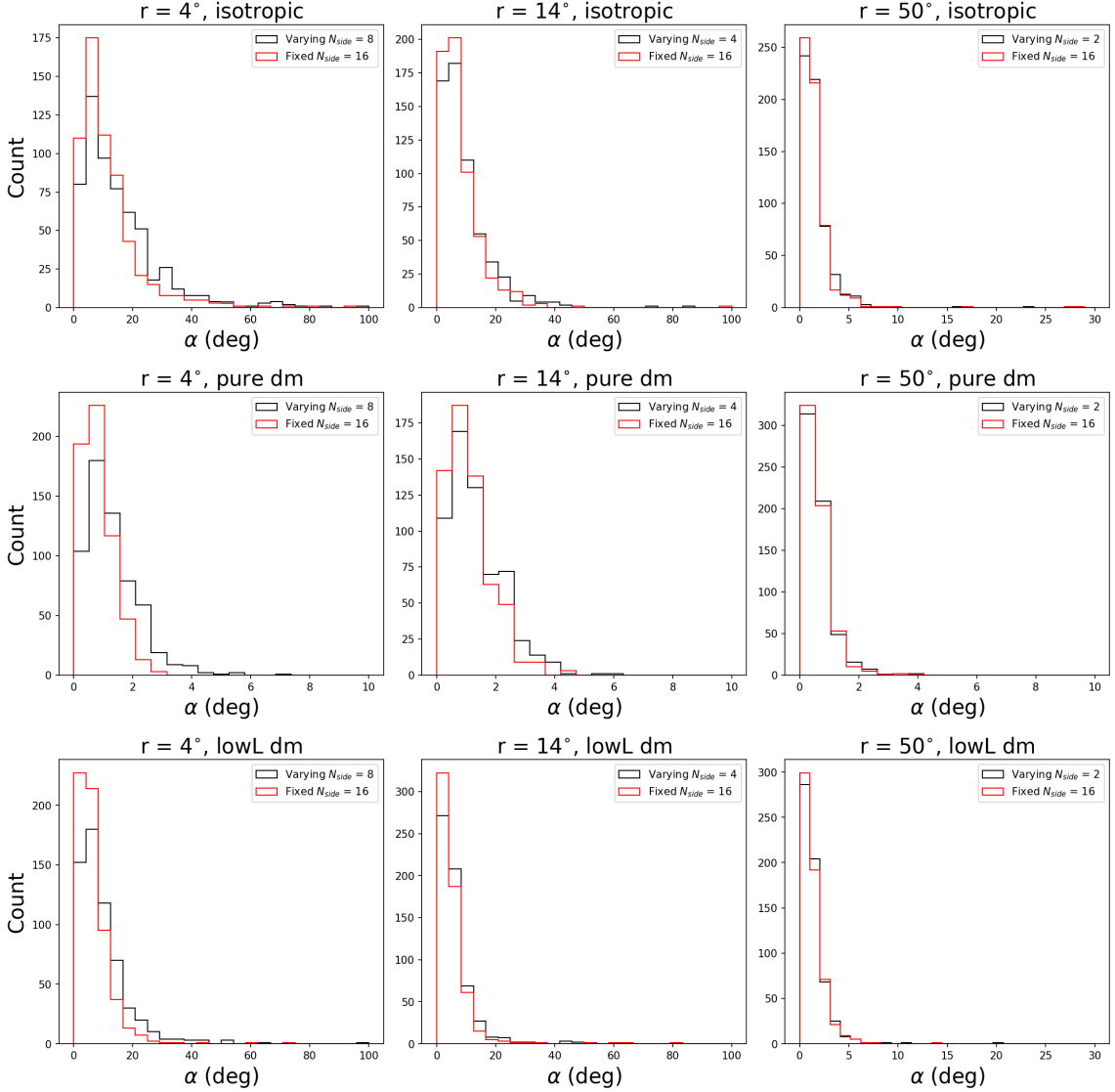


Figure A.3: Histogram of angular separation between dipole directions recovered from LVE maps as estimated using a simple fit and an inverse variance weighting in varying  $N_{\text{side}}$  (black) or fixed  $N_{\text{side}}=16$  (red) cases for some select disc sizes.

expectantly Gaussian random fluctuations on sky. Thus the variance of individual pixels in an LVE map differs. Therefore we would get a better fit for the dipole, if we employ a weighted fit to estimate the dipole from normalized LVE maps. For this *inverse variance weighted fit*, we use the same HEALPix’s `remove_dipole` function but will now make use of the inverse of the diagonal elements of the corresponding covariance matrix per Eq. (12) as weights to get dipole estimates.

In Section 4.1, we have already shown the covariance matrices and the corresponding correlation matrices that highlights the need for a weighted fitting using the diagonal elements of the covariance matrix for a particular choice of disc radii. We have also shown that using different  $N_{\text{side}}$  for deriving LVE maps for different choices of disc radii, there will be minimum to no correlations between LVE map pixels. With this in mind, we do the inverse variance fitting of LVE maps to estimate the underlying dipole using the diagonal elements of covariance matrix corresponding to that choice of disc radius ‘ $r$ ’ and  $N_{\text{side}}$ . We also do that same for the fixed  $N_{\text{side}}=16$  case in our comparison that follows.

In Fig. [A.1], we show the recovered dipole amplitude and directions for disc radii  $4^\circ$ ,  $14^\circ$ ,



and  $50^\circ$  from isotropic simulations (first and second rows), pure dipole modulated simulations (third and fourth rows) and low multipole only dipole modulated maps (fifth and sixth rows), respectively in the first, second and third columns. They are obtained following the two dipole fitting schemes described above. *Red* colour is reserved for  $N_{\text{side}}=16$  case and *black* is used for varying  $N_{\text{side}}$  outcomes. The vertical line in *magenta* with  $A = 0.072$  represents the amplitude of dipole used to simulate dipole modulated maps. As such there is no major variation in the directions and amplitudes of the recovered dipole from normalized LVE maps using the two schemes. This could be because the diagonal elements of the covariance matrices of LVE maps for any disc radii are not very different. Indeed from their histograms we find that most of the diagonal elements are located around the same value or have nearly same order of magnitude. Hence a simple fit equivalent to a least square fit is resulting in similar estimates for LVE maps' dipoles in comparison to using inverse variance weighting. This in turn could be a consequence of the fact that CMB temperature maps are signal dominated. However this might be very relevant in case of polarization analysis where even the latest full sky measurements from *Planck* are noise dominated. In Fig. [A.2] we present the same results but for the fixed  $N_{\text{side}}=16$  case. Our observations for the case of varying  $N_{\text{side}}$  remain valid here also.

Now in order to understand the difference in the dipole direction recovered when using simple fitting ( $\hat{d}_s$ ) versus inverse variance weighting fit ( $\hat{d}_w$ ), we compute the angular separation between the two dipole directions thus recovered as  $\alpha = \cos^{-1}(\hat{d}_s \cdot \hat{d}_w)$ . We do so in both cases of fixed  $N_{\text{side}}=16$  and varying  $N_{\text{side}}$  LVE maps. The results are presented in Fig. [A.3] as found in isotropic (top row), pure dipole modulated (middle row) and low- $l$  dipole modulated (bottom row) CMB maps. Column-wise, the histograms of angular separation between dipole directions from a simple fit and inverse variance weighting fitting are shown for select disc radii of  $r = 4^\circ$  (first column),  $14^\circ$  (second column) and  $50^\circ$  (third column). This angular separation ' $\alpha$ ' between the two schemes to fit the dipole from LVE maps for both cases of varying  $N_{\text{side}}$  (in *black* color) and fixed  $N_{\text{side}}=16$  (in *red* color) are exhibited in each subplot. It is obvious from the figure that in most cases we recover the same direction whichever dipole fitting scheme is employed whether in isotropic or modulated simulations, though there seem to exist some outliers. Further there is again no major difference in the using fixed  $N_{\text{side}}$  or varying  $N_{\text{side}}$  grids in generating local variance maps for a particular disc radii. Again this may be a consequence of the signal dominated CMB temperature data. This aspect should however be tested further in case of polarization data analysis.

Thus we have decided upon using the inverse variance weighing scheme to fit the dipole from LVE maps in this work. We will now try to find the distribution of the recovered dipole direction at different disc radii in the range  $r = 1^\circ$  to  $90^\circ$  comparing the two cases of fixed  $N_{\text{side}}=16$  and the varying  $N_{\text{side}}$ .